Universitat
de les Illes Balears

Following up the First Detection of Gravitational Waves with Numerical Relativity Simulations

Alfred Castro Ginard

Master's Thesis

Master's degree in Physics
(With a speciality/Itinerary in Astrophysics and Relativity)

at the

UNIVERSITAT DE LES ILLES BALEARS

Academic year 2015-16

Date: September, 2016

Author signature

UIB Master's Thesis Supervisor Dr. Sascha Husa

Supervisor signature

Abstract

The first detection of a gravitational wave signal occurred on September 14 2015, when the two LIGO detectors in Hanford and Livingston registered a consistent signal with a statistical significance of more than 5σ relative to the background noise. In order to identify the source of gravitational wave signals, they need to be compared with theoretical predictions. In the case of the first detection, the signal was found consistent with the prediction of general relativity for the waves produced by the last orbits and coalescence of two black holes with initial masses $36M_\odot$ and $29M_\odot$, leading to a final black hole mass of $62M_\odot$ with $3.0M_\odot c^2$ radiated in gravitational waves. The modern theory of gravitation is Einstein's theory of general relativity, and modelling possible signals with solutions of the Einstein equations is a key goal for gravitational wave physics. Perturbative methods, as have been used for the indirect discovery by Hulse, Taylor, and Weisberg [1, 2] of gravitational wave emission from the binary pulsar PSR B1913+16 in 1974, break down in the strong field regime of general relativity, and to model the merger of black holes, the methods of numerical relativity to solve the Einstein equations without physical approximations need to be used.

In this thesis a precessing waveform compatible with the first detection event, GW150914, is constructed by numerical solution of the Einstein field equations as a system of coupled nonlinear partial differential equations, and compared with the data recorded by the LIGO detectors. Perturbative methods are used to compute initial parameters for the black holes, and to construct a complete waveform by matching the numerical and perturbative solutions. Physical properties of the solution are computed and discussed, such as the final spin, final mass, recoil velocity and energy distribution for different spherical harmonic modes of the wave signal.

The Einstein evolution equations can be considered a nonlinear system of wave equations, and the numerical solution of the linear wave equation is discussed to introduce the numerical finite difference methods used.

Acknowledgements

I would like to thank to my thesis advisor, Dr. Sascha Husa, for giving me the opportunity to work with him, the guidance and patience during these years.

I would also like to thank to Xisco Jiménez Forteza, for his helpful talks and for the time we spent working together. Also thank to my office partner, Pep Covas, for his useful contributions during this year.

Also, thank to all the LIGO@UIB group, specially to Dr. Alicia Sintes and Dr. David Keitel for their valuable suggestions.

Finally, thank to the Institute of Applied Computing with Community Code (IAC^3) for giving me their introduction to research scholarship.

To my parents

Contents

1 Introduction **1**

2 Black Holes, Binaries and Gravitational Waves **5**

2.1 Schwarzschild Geometry 6

2.2 Kerr Geometry 6

2.3 Horizons 7

2.3.1 Trapped Surfaces and Apparent Horizons 7

2.4 Black Hole Binaries 8

2.5 Gravitational Waves 9

3 Effective One-Body approach **11**

3.1 Orbital Hamiltonian 11

3.2 Spin contribution 12

3.3 Equations of motion and conserved quantities 13

3.4 Radiation Reaction 14

4 Mathematical Procedure **17**

4.1 Initial Value Problem 17

4.1.1 Well-posedness 18

4.2 The *3+1 Decomposition* 18

4.2.1 Extrinsic Curvature 21

4.2.2 Decomposition of the Riemann tensor 22

4.3 The York-ADM equations 24

4.4 The BSSN equations 24

5 Numerical Procedure **29**

5.1 Initial Data 29

5.2 Evolution 31

5.2.1 Conformal factor 32

5.2.2 Gauge conditions 33

5.3 Numerical Method 33

5.3.1 Evolution Method 34

5.3.2 Adaptive Mesh Refinement 34

5.3.3 Extraction quantities 35

5.4 Wave equation as a Toy Model for Hyperbolic Equations 39

6 Numerical Simulations of a Precessing $q = 1.2$ Black Hole Binary **45**

6.1 Runs Configuration 46

6.1.1 Convergence Test 49

6.1.2 Richardson Extrapolation 51

6.2 Precession 52

6.3 Results 53

6.3.1 Final Mass and final spin 55

6.3.2 Final Recoil Velocity 56

6.4 Waveform 57

6.4.1 Ψ_4 58

6.4.2 Fixed Frequency Integration (FFI) Method 59

7 The Detected Gravitational Wave Signal **63**

7.1 Spin Weighted Spherical Harmonics 64

7.2 Gravitational Wave Signal in the Detector Frame 64

7.2.1 Sky Location 66

7.2.2 The Detected Wave 68

7.3 GW150914 Data Analysis 69

7.4 Comparison to Real Data 71

8 Conclusions **75**

Bibliography **77**

Chapter 1

Introduction

Albert Einstein's theory of General Relativity (GR) [3] provides a different description of gravitation than Newtonian gravity, mathematically and conceptually. It starts from the fact that acceleration of the objects is not due to a force but due to the geometry of the space-time itself.

In Newtonian mechanics, the force of gravity can be described in terms on its gravitational potential ϕ, that comes from a continuous mass distribution ρ, defined using the Laplace operator as,

$$\Delta\phi = 4\pi G\rho. \tag{1.1}$$

In GR, gravity is not a force but geometry, the gravitational potential ϕ is replaced by the metric tensor g_{ab}, which contains the information of the geometric structure of the space-time: and the mass distribution ρ is now replaced by the distribution of matter and energy, the stress-energy tensor T_{ab}. The sources of the curvature and the space-time's geometry can be related with the Einstein field equations, and, equation (1.1) can be replaced by,

$$G_{ab} = \frac{8\pi G}{c^4} T_{ab}, \tag{1.2}$$

where the Einstein tensor G_{ab}, defined as $G_{ab} = R_{ab} - \frac{1}{2}Rg_{ab}$, depends on the metric tensor, so it describes the geometry of the space-time. The indices $\{a, b\}$ goes from zero to three denoting the different temporal (0) and spatial (1-3) dimensions. So, the problem of modelling the evolution of a black hole binary consists in solving the Einstein vacuum equations ($R_{ab} = 0$).

On one hand, in Newtonian gravity, the interaction of two point masses represents the simplest non-trivial problem, it describes a wide range of physical situations, and, in

addition, it can be solved analytically. On the other hand, GR presents a more complicate and completely new theory. In General Relativity, as it is known, the two body problem loses energy which is radiated as gravitational radiation that propagates away from the source as waves at the speed of light. Thus, the two body problem in GR is unstable, and it will result in the shrink of the orbit that will lead to the collision of the two objects. Gravitational waves are generated by accelerated masses, and, the most massive and accelerated the objects are, the most energetic gravitational waves they will emit. To generate such gravitational waves, the two objects need to be massive objects orbiting at very close separations. So, now, the most compact objects are not point particles anymore but black holes. The study of the two body problem has now become to the study of a black hole binary.

The two body problem now represents a huge challenge, from considering an ordinary differential equation (ODE) in Newtonian Gravity and find its solution; to numerically solve, in GR, a set of ten coupled, non-linear second order partial differential equations (PDE's).

The field of Numerical Relativity is dedicated to the construction of black hole spacetimes by numerically integrating the Einstein's equations (1.2). The first attempt of solving them, for two black holes, was done by Hahn and Lindquist in 1964 [4], but at the time, although they knew a procedure for the numerical integration, due to insufficient computational resources, inadequate gauge conditions and the lack of a well-posed formulation, they could only evolve their data for a short time. Significant breakthrough was made at 2005 when the first numerical simulations that include the merger and ringdown phases were carried out by Pretorius [5]. Since then, simulations of black hole binaries in the field of Numerical Relativity have given a better insight into the dynamics of binary black hole coalescence.

The motivation in the effort of the Numerical Relativity in modelling gravitational wave sources comes from the construction of gravitational wave detectors such as LIGO [6], VIRGO [7] or GEO600 [8]. Waveform catalogues, a library that contains waveforms coming from different black hole configurations which patterns are searched in the real data, have helped gravitational waves data analysis teams to report the first direct detection of a gravitational wave, GW150914 [9], by the LIGO Scientific Collaboration on September 14, 2015. However, Numerical Relativity is not the only field dedicated to the construction of waveform templates, the signal in the sensitivity band of the detector covers many

more orbits than those modeled by Numerical Relativity simulations. Those orbits can be modeled by analytical Post-Newtonian methods, or using *effective one-body* models because the evolution in the early inspiral stage is adiabatic. Then, the waveform is constructed by stitching together analytical waveforms with numerical ones.

This thesis will cover the process of the construction of a precessing waveform model, whose parameters are consistent with GW150914 [10]. Some basic aspects of black holes and gravitational waves needed in this thesis will be covered in Chapter 2. An analytical approach to the first inspiral phase of the binary evolution is given in Chapter 3. A mathematical description of how to get the Einstein field equations in the $3+1$ form will be explained in Chapter 4. The numerical code used to evolve the black hole binary is described in Chapter 5. Chapter 6 goes through the numerical simulation of the binary black hole merger and it's results. And finally, a comparison of the waveform constructed and the real data recorded by the detectors is performed in Chapter 7.

Chapter 2

Black Holes, Binaries and Gravitational Waves

We can see the light coming out from a star like our Sun because the speed of light is higher than the escape velocity of the star, given by,

$$v_e = \sqrt{\frac{2GM}{R}}, \tag{2.1}$$

where we see how compact is the star in the relation between its mass and radius M/R. If we invert the problem and see what size the star should have, so that the light can not escape, in the case of our Sun, it would be a radius of about 3km, computed by just inverting equation (2.1), $R = \frac{2GM}{c^2}$.

When one considers the time evolution of the given star, it will eventually run out of nuclear fuel, consequently, the star will not be able to maintain the equilibrium; so, the star will undergo gravitational collapse. Nevertheless, because of the contraction, the star may change its equation of state, leading to a new equilibrium state. These new equilibrium states can be supported by Fermi pressure of the electrons (white dwarfs) or the neutrons (neutron stars). But when we solve the Tolman-Oppenheimer-Volkoff (TOV) equations, we see that for a given equation of state there is a maximum mass for the star to be in equilibrium. Because that mass is so large, the Newtonian equation (2.1) gives us velocities higher than the speed of light. To solve that problem, we need to approach the situation from the point of view of the General Relativity.

2.1 Schwarzschild Geometry

When a spherically symmetric star has collapsed, the whole space-time can be described with the Schwarzschild geometry, which is the most general vacuum solution of the Einstein field equations.

The Schwarzschild geometry [11] is an exact solution to the Einstein field equations (1.2) found shortly after their publication by Karl Schwarzschild. The form of the metric is

$$ds^2 = -\left(1 - \frac{2M}{r}\right) dt^2 + \left(1 - \frac{2M}{r}\right)^{-1} dr^2 + r^2(d\theta^2 + \sin^2(\theta) d\varphi^2), \tag{2.2}$$

note the use of geometric units ($G = c = 1$) that will be used from now on. At $r = 0$ and $r = 2M$ the metric coefficients g_{tt} and g_{rr} become zero or infinite, but because metric coefficients are coordinate dependent, these singularities could be an effect of the choice of the coordinates, or it could be real singularities in the space-time. To distinguish between both possibilities one have to find a scalar quantity, which is coordinate independent, such as the Riemann Scalar $R^{abcd}R_{abcd}$ and see whether it behaves singular or not. For the Schwarzschild metric (2.2), one can see,

$$R^{abcd}R_{abcd} = \frac{48M^2}{r^6}, \tag{2.3}$$

that $r = 0$ represents a true singularity.

However, the feature that defines a black hole is not its singularity at $r = 0$ but at $r = 2M$, where the event horizon forms. The event horizon is null hypersurface which is a boundary in the space-time within which the gravitational attraction is so strong than not even light can escape from it. The description above is for a Schwarzschild black hole, that thanks to the Birkhoff theorem we know this is the only solution for the space-time outside a spherical, non-rotating, gravitating body that would result from an spherical gravitational collapse. But not only this kind of collapse leads to the formation of a black hole. Nevertheless, the basic picture of the collapse when no spherical simplifications can be applied would remain the same and a black hole would form.

2.2 Kerr Geometry

One can find a more general family of solutions of (1.2) that leads to the existence of black holes. The no-hair theorem [12] states that all black hole solutions can be described in

terms of three parameters: mass (M), angular momentum (J) and charge (Q). Given that most of the astrophysical objects are neutral ($Q = 0$), a solution in terms of $\{M, J\}$ is given by the Kerr metric, that describes the geometry around a rotating black hole, it can be written as,

$$ds^2 = -\left(1 - \frac{2Mr}{\rho^2}\right) dt^2 - \frac{4Mar\sin^2(\theta)}{\rho^2} dt d\varphi + \frac{\rho^2}{\Delta} dr^2 + \rho^2 d\theta^2 + \frac{\sin^2(\theta)}{\rho^2}\left((r^2 + a^2)^2 - a^2\Delta\sin^2(\theta)\right) d\varphi^2, \tag{2.4}$$

where $\rho^2 = r^2 + a^2\cos^2(\theta)$; and $\Delta = r^2 - 2Mr + a^2$; and the Kerr parameter a is defined by $a = J/M$.

In this metric, we find again singular points when $\rho = 0$ and $\Delta = 0$. If we analyse these points analogously to the Shcwarzschild case, the evaluation of the Riemann scalar $R^{abcd}R_{abcd}$ shows that $\rho = 0$ is a true singularity, just as $r = 0$ in the Schwarzschild geometry. Thus, the singularity at $\Delta = 0$ is a coordinate singularity and, analogous to the Schwarzschild case, indeed turns out to be the event horizon.

2.3 Horizons

So far we have just mentioned the event horizon, a region of the space-time that encloses a singularity, and where not even light can escape from it. But from the definition, the event horizon is about the ultimate fate of the observer, it can only be determined if the maximal time development is known. However, it would be useful to describe a similar region but locally in time, so one won't have to wait till the end of time to locate the horizon. That is the notion of a trapped surface and the apparent horizon.

2.3.1 Trapped Surfaces and Apparent Horizons

Imagine a sphere in a spatial slice of the space-time Σ of constant time coordinate. If we send photons from the sphere surface (S), a light cone will be formed as the photons propagates away from the surface at later times. If the spherical surface encloses a singularity the curvature of the space-time around may be so strong that eventually the path of the outgoing photon may also bend.

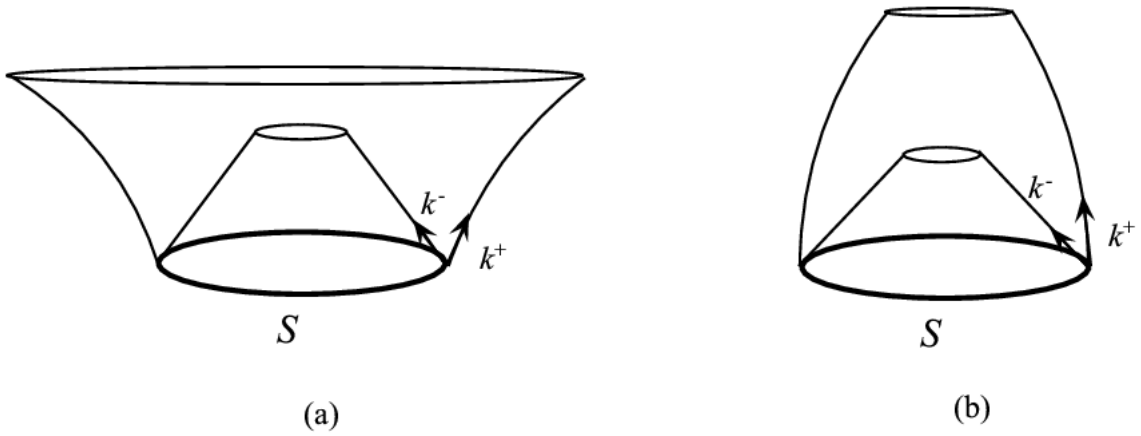

Figure 2.1: Notion of untrapped (a) and trapped surfaces (b). k^- and k^+ are the null-vectors associated to the ingoing and outgoing front. Source: https://inspirehep.net/record/1279001/plots

When the rate of change of the area generated by the outgoing front is negative, then we have a trapped surface. The notion of an apparent horizon in derived from the trapped surface: the boundary of the regions of trapped surfaces. So, we define the marginally outer trapped surface (MOTS), represented by the outgoing photon front, when the rate of change of the area generated by the outgoing front becomes zero. And we identify the MOTS as the apparent horizon which is defined at every spatial hypersurface Σ.

Therefore, black holes can be defined by its apparent horizon instead of its event horizon. This is an essential component of binary black hole evolution codes.

2.4 Black Hole Binaries

The most promising sources of gravitational waves are two black holes orbiting each other forming a bound system. As already mentioned, the two-body problem in GR is not stable, the binary radiates away energy and momentum in the form of gravitational waves resulting in the decay of the orbits until both black holes merge together.

The evolution of a black hole binary goes through three different processes as each black hole moves towards the other. A first, extended phase where the radiation of energy makes the binary adiabatically evolve to smaller separations which is called **inspiral**. The **merger**, where the gravitational wave emission is no longer adiabatic and both black holes plunge together and merge. And the last stage, when a single Kerr black hole is formed which is called **ringdown**.

During the inspiral stage, when the two black holes are far enough to be modulated by the Post-Newtonian approximation, gravitational wave emission will remove energy from the binary causing the decrease of the separation of the black holes. At this stage, an analytical approach to the radiated power and thus, to the evolution of the binary separation and to the amplitude of the gravitational waves emitted can be performed using the Post-Newtonian expansion. At the leading order, this energy loss can be modeled by the quadrupole formula as

$$\frac{dE}{dt} = -\frac{G}{5c^5}\sum_{i,j}\left(\frac{d^3Q_{ij}}{dt^3}\right)^2, \tag{2.5}$$

where $Q_{ij} = \int \rho(x_i x_j - \delta_{ij} r^2/3)\mathrm{d}^3x$ is the mass quadrupole moment.

At the ringdown stage, the remnant black hole can be described as a perturbed Kerr black hole. It has been realized that perturbed black holes have quasi-normal modes of vibration, which are the formal solutions of the linearized differential equations of the General Relativity with complex frequency; and the gravitational waves emitted from the merger can be described as a superposition of these quasi-normal modes, and computed using perturbative techniques [13, 14].

It is during the merger, where the need of computational resources appear. The accurate modelling of this stage is done via Numerical Relativity simulations.

2.5 Gravitational Waves

Another exciting prediction of the General Relativity is the existence of gravitational waves. They are perturbations of the space-time propagating away from the source as waves at the speed of light, generated by non-spherical or nonuniform mass in motion.

Gravitational Waves carry energy as gravitational radiation. Even Gravitational Waves can transport large amounts of energy, they interact very weakly with matter, that is the reason why they are so difficult to detect but at the same time this fact allow them to travel storing the information of the source unaffected. One can see this weakness in (2.5) with the dependence of the constants G and c, and also comparing the gravitational radiation to the electromagnetic radiation, which its leading order is the dipole instead of the quadrupole moment.

The first indirect detection of Gravitational Waves was the observation of the orbital decay of the Hulse-Taylor binary system [1], the energy loss through the emission of gravi-

tational radiation is consistent with the prediction of General Relativity. Since then, many efforts have been made to directly detect Gravitational Waves. Ground-based interferometric detectors such as LIGO [6], VIRGO [7], GEO600 [8] have been built resulting in the first direct detection of Gravitational Waves emitted in a binary black hole coalescence [9]. Gravitational waves are detected via interferometric techniques measuring the relative change in the detector's arms $\Delta L/L$ of length L, see Chapter 7.

Accurate numerical simulations of black hole binaries allow the creation of waveforms catalogues, so one can compare to the real data recorded by the detectors and identify the better gravitational wave model that best represents the data. In further chapters, the waveform emitted by the merger will be constructed via full numerical Relativity. Nevertheless, we can see with simple arguments why it should be a binary black hole [15]. Those arguments are: (i) the frequency and amplitude of the gravitational wave are increasing, this suggest that it should come from the orbital motion of a binary; and (ii) the maximum frequency at which the gravitational radiation is observed tells us how close the orbiting objects should be, only black holes can reach such a small separation.

Chapter 3

Effective One-Body approach

In the last moments of a binary black hole coalescence, the Einstein field equations have to be solved via full Numerical Relativity (NR). However, there is no need to solve those equations from the beginning, where the two black holes are adiabatically inspiralling together, since the simulations would be very computational expensive. The time to the coalescence goes as [16]

$$t_{coal} \propto \omega^{-3/8}, \tag{3.1}$$

where ω is the frequency of the gravitational wave.

To avoid this extra cost, we can use analytical, approximate, descriptions of the transition between the adiabatic inspiral to the plunge thanks to the effective one-body (EOB) approach [17], and in addition the result of the EOB approach will give us initial data for the NR simulation that will yield to a more robust evolution. The EOB approach has been used to derive templates of waveforms emitted from a non-spinning binary black hole [18] and also for the case of spinning black holes [19]. It has also been already extended when there is precession [20], case which is going to be followed in this section.

3.1 Orbital Hamiltonian

The effective one-body approach, defines a specific re-summation of the PN-expanded Hamiltonian that leads to a much more reliable description of the dynamical evolution near the innermost stable circular orbit (ISCO), and of the transition between inspiral and plunge; and a re-summed version of radiation reaction. A re-summation is used because

the Post-Newtonian expansion is a divergent serie, so the *ansatz* (3.2) is used to re-define the PN-expansion in terms of the EOB hamiltonian that describes the early inspiral stages and the spin effects.

The first contribution, the pure orbital Hamiltonian, described in terms of canonical variables $(\mathbf{X'}, \mathbf{P'})$, takes the form

$$H^0_{EOB}(\mathbf{X'}, \mathbf{P'}) = M\sqrt{1 + 2\eta\left(\frac{H_{eff}(\mathbf{X'}, \mathbf{P'}) - \mu}{\mu}\right)} - M, \tag{3.2}$$

where μ is the reduced mass $\mu = m_1 m_2/M$ in terms of the individual black hole masses and the total mass; η is the symmetric mass ration $\eta = \mu/M$; and the H_{eff} is given by

$$\begin{aligned} H_{eff}(\mathbf{X'}, \mathbf{P'}) &= \mu\hat{H}_{eff}(\mathbf{q'}, \mathbf{p'}), \\ &= \mu\sqrt{A(q')\left(1 + \mathbf{p'}^2 + \left(\frac{A(q')}{D(q')} - 1\right)(\mathbf{n'}\cdot\mathbf{p'})^2 + \frac{1}{\mathbf{q'}^2}(z_1(\mathbf{p'}^2)^2 + z_2\mathbf{p'}^2(\mathbf{n'}\cdot\mathbf{p'})^2 + z_3(\mathbf{n'}\cdot\mathbf{p'})^4)\right)}, \end{aligned} \tag{3.3}$$

where we obtain the reduced canonical variables $(\mathbf{q'}, \mathbf{p'})$ by re-scaling $(\mathbf{X'}, \mathbf{P'})$ by M and μ, respectively, and define $\mathbf{n'} = \mathbf{q'}/q'$ where $q' = |\mathbf{q'}|$. The coefficients z_1, z_2 and z_3 are arbitrary, subject to the constraint

$$8z_1 + 4z_2 + 3z_3 = 6(4 - 3\eta)\eta. \tag{3.4}$$

Different expressions for $A(q')$ and $D(q')$ can be found in [20] up to 2PN and 3PN orders.

3.2 Spin contribution

Taking the orbital contribution as the leading order, we can just add the spin contributions by adding more terms to the Hamiltonian,

$$H_{EOB}(\mathbf{X}, \mathbf{P}, \mathbf{S}_1, \mathbf{S}_2) = H^0_{EOB}(\mathbf{X}, \mathbf{P}) + H_{SO}(\mathbf{X}, \mathbf{P}, \mathbf{S}_1, \mathbf{S}_2) + H_{SS}(\mathbf{X}, \mathbf{P}, \mathbf{S}_1, \mathbf{S}_2), \tag{3.5}$$

where

$$H_{SO} = 2\frac{\mathbf{S}_{eff}\cdot\mathbf{L}}{R^3}, \tag{3.6}$$

$$H_{SS} = H_{S_1S_1} + H_{S_1S_2} + H_{S_2S_2}. \tag{3.7}$$

If we focus on the spin-orbit contribution H_{SO}, where

$$\mathbf{S}_{eff} = \left(1 + \frac{3}{4}\frac{m_2}{m_1}\right)\mathbf{S}_1 + \left(1 + \frac{3}{4}\frac{m_1}{m_2}\right)\mathbf{S}_2, \tag{3.8}$$

and $\mathbf{L}$ is the angular momentum given by $\mathbf{L} = \mathbf{x} \times \mathbf{p}$. If we compare with a potential of the form $V = -M/R$ which is attractive, we can see the contribution of the spin-orbit term by analyzing two extreme cases: if $\mathbf{S}$ is parallel to $\mathbf{L}$ then H_{SO} will be a repulsive term, leading to the radiation of more energy since the binary will take more orbits to merge. While if $\mathbf{S}$ and $\mathbf{L}$ are anti-parallel we will have the opposite case.

The spin-spin contribution takes the form

$$H_{SS} = \frac{\mu}{2MR^3}(3(\mathbf{S}_0 \cdot \mathbf{N})(\mathbf{S}_0 \cdot \mathbf{N}) - (\mathbf{S}_0\mathbf{S}_0)), \tag{3.9}$$

with

$$\mathbf{S}_0 = \left(1 + \frac{m_2}{m_1}\right)\mathbf{S}_1 + \left(1 + \frac{m_1}{m_2}\right)\mathbf{S}_2, \tag{3.10}$$

and $\mathbf{N} = \mathbf{X}/|\mathbf{X}|$. The terms $H_{S_1S_1}$, $H_{S_1S_2}$ and $H_{S_2S_2}$ originate from the interaction of the monopole m_2 with the spin-induced quadrupole moment of the spinning black hole of mass m_1 and vice versa. The expressions for this terms are,

$$H_{S_1S_2} = \frac{1}{R^3}(3(\mathbf{S}_1 \cdot \mathbf{N})(\mathbf{S}_2 \cdot \mathbf{N}) - (\mathbf{S}_1 \cdot \mathbf{S}_2)), \tag{3.11}$$

$$H_{S_1S_1} + H_{S_2S_2} = \frac{1}{2R^3}(3(\mathbf{S}_1 \cdot \mathbf{N})(\mathbf{S}_1 \cdot \mathbf{N}) - (\mathbf{S}_1 \cdot \mathbf{S}_1))\frac{m_2}{m_1} + \frac{1}{2R^3}(3(\mathbf{S}_2 \cdot \mathbf{N})(\mathbf{S}_2 \cdot \mathbf{N}) - (\mathbf{S}_2 \cdot \mathbf{S}_2))\frac{m_1}{m_2}. \tag{3.12}$$

The H_{SS} term has the opposite effect that H_{SO} has on the orbital motion.

3.3 Equations of motion and conserved quantities

In general, we can find the time evolution for a quantity of the form $f(\mathbf{X}, \mathbf{P}, \mathbf{S}_1, \mathbf{S}_2)$ using the definition

$$\frac{d}{dt}f(\mathbf{X}, \mathbf{P}, \mathbf{S}_1, \mathbf{S}_2) = \{f, H\}, \tag{3.13}$$

where the term on the right hand side denote the Poisson brackets $\{X^i, P_j\} = \delta^i_j$. Given the Hamilton equations,

$$\frac{d\mathbf{X}}{dt} = \frac{\partial H}{\partial \mathbf{P}}, \tag{3.14}$$

$$\frac{d\mathbf{P}}{dt} = -\frac{\partial H}{\partial \mathbf{X}}, \tag{3.15}$$

the motion for the spins can be derived as,

$$\frac{d}{dt}\mathbf{S}_1 = \{\mathbf{S}_1, H\} = \frac{\partial H}{\partial \mathbf{S}_1} \times \mathbf{S}_1 = \Omega_1 \times \mathbf{S}_1 \tag{3.16}$$

$$\frac{d}{dt}\mathbf{S}_2 = \{\mathbf{S}_2, H\} = \frac{\partial H}{\partial \mathbf{S}_2} \times \mathbf{S}_2 = \Omega_2 \times \mathbf{S}_2 \tag{3.17}$$

where

$$\Omega_1 = \left(2 + \frac{3}{2}\frac{m_2}{m_1}\right)\frac{\mathbf{L}}{R^3} + \frac{1}{R^3}(3\mathbf{N}(\mathbf{S}_2 \cdot \mathbf{N}) - \mathbf{S}_2) + \frac{3}{R^3}\frac{m_2}{m_1}\mathbf{N}(\mathbf{S}_1 \cdot \mathbf{N}), \tag{3.18}$$

$$\Omega_2 = \left(2 + \frac{3}{2}\frac{m_1}{m_2}\right)\frac{\mathbf{L}}{R^3} + \frac{1}{R^3}(3\mathbf{N}(\mathbf{S}_1 \cdot \mathbf{N}) - \mathbf{S}_1) + \frac{3}{R^3}\frac{m_1}{m_2}\mathbf{N}(\mathbf{S}_2 \cdot \mathbf{N}). \tag{3.19}$$

If there is no radiation reaction, we can derive from the equations of motion that the energy $E = H$ and the total angular momentum $\mathbf{J} = \mathbf{L} + \mathbf{S}_1 + \mathbf{S}_2$ will be preserved.

Considering just the leading spin-orbit term, the equation for the angular momentum takes the form,

$$\frac{d\mathbf{L}}{dt} = \frac{2}{R^3}\mathbf{S}_{eff} \times \mathbf{L}. \tag{3.20}$$

3.4 Radiation Reaction

Including radiation reaction effects within the Hamiltonian approach means to modify the equations (3.14,3.15) such that,

$$\frac{dX^i}{dt} = \{X^i, H\} = \frac{\partial H}{\partial P_i}, \tag{3.21}$$

$$\frac{dP^i}{dt} = \{P^i, H\} + F_i = -\frac{\partial H}{\partial X^i} + F_i, \tag{3.22}$$

where F_i is a non-conservative force added to the evolution equation of the momentum to take into account radiation reaction effects. This force depends on the orbital variables $\mathbf{X}$, $\mathbf{P}$ and on the spins $\mathbf{S}_1$ and $\mathbf{S}_2$.

In the presence of precession, when the spins are not aligned with the orbital angular momentum, and, including radiation reaction effects, $\mathbf{L}$ is going to get smaller because of the energy loss.

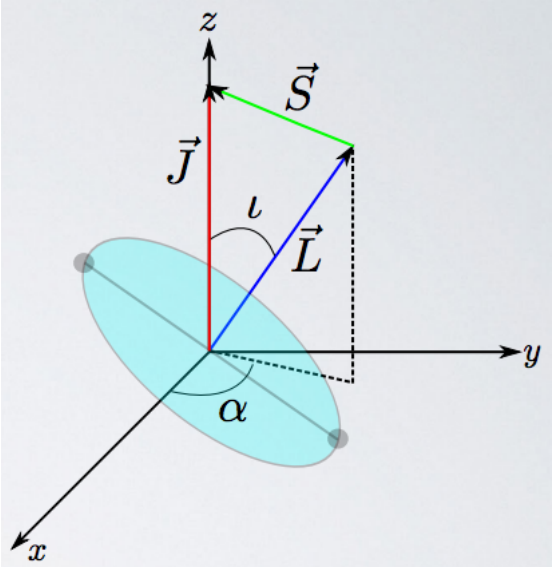

Figure 3.1: Total angular momentum $\boldsymbol{J}$ *as the sum of* $\boldsymbol{L}$ *and* $\boldsymbol{S} = \boldsymbol{S}_1 + \boldsymbol{S}_2$. *Source: http://hyperphysics.phy-astr.gsu.edu/hbase/quantum/vecmod.html.*

The angle ι between **J** and **L** will evolve in time according to

$$\cos\iota = \frac{S_L + L}{\sqrt{S_p^2 + (S_L + L)^2}}, \tag{3.23}$$

where S_L and S_p are the projections normal and parallel to **L**. This will lead to simple precession (when J is preserved) or transitional precession (when J changes and eventually goes through zero).

Chapter 4

Mathematical Procedure

Beyond the inspiral, the merger and ringdown of a binary black hole coalescence and computing the gravitational radiation emitted requires numerical simulations to model these stages where both black holes plunge together and ends forming a single Kerr black hole.

But such a numerical simulation consists in evolving in time a set of equations that carry information about the spatial structure for a given initial data. However, the Einstein field equations (1.2) are written in a co-variant way, where no distinction between space and time is made and the whole set of coordinates is treated the same way, a formalism to separate the coordinates in a way that allow us to obtain the evolution needs to be done.

There are different approaches to separate Einstein field equations in a way that we can perform a numerical evolution from given initial data, specific formalisms differ in the way that the separation is carried out. In this section we will focus in the *3+1 formalism*, which is the most used in numerical relativity, but not the only one [21, 22].

4.1 Initial Value Problem

The aim of this section is to write the Einstein field equations as an initial value problem, *i.e.* find a solution $u(t, x)$ for all t from a given $u(0, x)$. The *3+1 formalism* leads to a set of evolution equations which are not unique. Different systems of *3+1* evolution equations will have the same physical solution but they will differ in their mathematical properties.

Our goal is to find a system of equations that is well behaved both mathematically and numerically. In order to achieve that, it has been found that the whole system of evolution

equations has to be well-posed.

4.1.1 Well-posedness

Once the Einstein field equations are written as an initial value problem, we want it to be well-posed. If appropiate initial data $u(0)$ is defined at $t = 0$, then, in a well-posed system a unique solution can be found for all the posterior times $u(t)$, and it depends continuously on the given initial data, *i.e.*

$$\|u(t)\| \leq K\mathrm{e}^{at} \|u(0)\| , \tag{4.1}$$

where K and a are constants that do not depend on the initial data. For a deeper insight see [23].

4.2 The *3+1 Decomposition*

Global hyperbolicity. We call a Cauchy hypersurface to an hypersurface Σ which domain of dependence is the whole space-time $\mathcal{M}$, $D(\Sigma) = \mathcal{M}$; a space-time which possesses a Cauchy hypersurface is called globally hyperbolic. Then, if $\mathcal{M}$ is globally hyperbolic, it allows a global time function t, such that each surface of constant t is a Cauchy surface; *i.e.* $\mathcal{M}$ can be foliated in surfaces Σ_t, see [24].

To write the Einstein field equations as a Cauchy problem, we start from a 4-dimensional globally hyperbolic space-time $\mathcal{M}$ where the metric g_{ab} measures coordinate distance between two space-time events,

$$ds^2 = g_{ab}dx^a dx^b, \tag{4.2}$$

and the curvature is measured using the notion of parallel transport leading to the Riemann tensor R_{abcd}.

The idea of the *3+1 formalism* is to split the 4-dimensional space-time $\mathcal{M}$ into a family of 3-dimensional space-like hypersurfaces of constant t, and see how the evolution variables of this formulation, the induced 3-dimensional metric and the extrinsic curvature, change in time. The description of how the $3 + 1$ decomposition is performed will follow the discussion given by Alcubierre in [25] in parallel with [26].

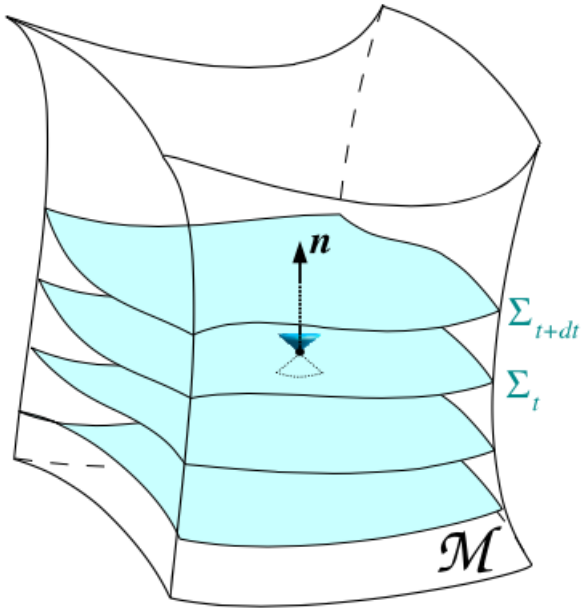

Figure 4.1: Space-time $\mathcal{M}$ split into 3-dimensional hypersurfaces of constant t. Source:[27].

As well as the metric g_{ab} measures the distance between two events in the space-time, one uses the **3-dimensional metric** γ_{ij} to measure distances within the hypersurface Σ_t itself,

$$dl^2 = \gamma_{ij} dx^i dx^j, \tag{4.3}$$

note the use of Latin indices to denote spatial coordinates. Again, analogously to g_{ab}, we also use γ_{ij} to raise and lower indices of pure spatial tensors.

We have to define two additional objects to move between different spatial hypersurfaces and cover the whole space-time: the **lapse function** $\alpha(t, x^i)$ which measures proper time between two hypersurfaces along n^a, that is a time-like vector normal to the hypersurface,

$$d\tau = \alpha(t, x^i) dt, \tag{4.4}$$

and the **shift vector** β^i, which is a vector tangent to Σ_t that measures the relative velocity between Eulerian observers (moving along n^a) and observers following a coordinate line (where $dx^i = 0$), Figure 4.2.

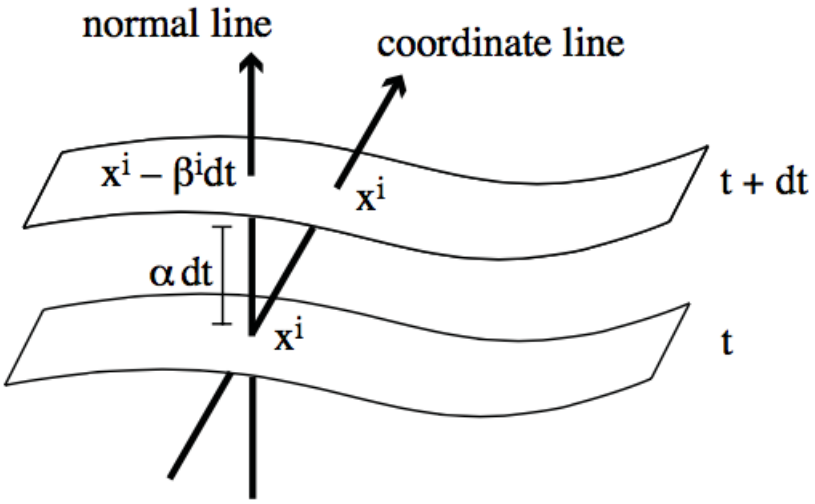

Figure 4.2: Visual definitions of the lapse function and the shift vector. Source:[25].

The unit vector n^a normal to the spatial hypersurfaces can be expressed in terms of the global time function t as,

$$n^a = -\alpha g^{ab} \nabla_b t, \tag{4.5}$$

where the minus sign indicates that n^a is pointing upward. It's normalized in such a way that the lapse function gets the form,

$$\begin{aligned} n^a n_a = -1 &= \alpha^2 g^{ab} (\nabla_a t)(\nabla_b t), \\ \alpha &= (-g^{ab}(\nabla_a t)(\nabla_b t))^{-1/2}, \end{aligned} \tag{4.6}$$

an expression for the shift vector can be found, since it's orthogonal to n^a, so it lies in Σ_t,

$$\beta^i = -\alpha(n^a \cdot \nabla x^i), \tag{4.7}$$

the most general way to go from one spatial hypersurface Σ_t to another Σ_{t+dt} would be,

$$t^a = \alpha n^a + \beta^a. \tag{4.8}$$

Both the lapse function and the shift vector can be freely specified and they are not unique. Our choice of the lapse will determine the slicing of the space-time just as the shift vector determines the spatial coordinates. They are known as the *gauge functions*.

The line element of the space-time in terms of the functions $\{\alpha, \beta^i, \gamma_{ij}\}$ takes the form,

$$ds^2 = g_{ab} dx^a dx^b = -\alpha^2 dt + \gamma_{ij}(dx^i + \beta^i dt)(dx^j + \beta^j dt), \tag{4.9}$$

and the components of the space-time metric as,

$$g_{ab} = \begin{pmatrix} -\alpha^2 + \beta_k\beta^k & \beta_i \\ \beta_j & \gamma_{ij} \end{pmatrix}. \tag{4.10}$$

Once the space-time is foliated we would like to project the Einstein equations into Σ_t to get the equations to evolve. We have to define a projection operator which is orthogonal to n^a, and it is nothing more than the induced 3-dimensional metric in each hypersurface by the full space-time metric,

$$\gamma_{ab} = g_{ab} + n_a n_b, \tag{4.11}$$

then, for example, if we want to define a co-variant derivative into Σ_t (D_a), that will do the same job in the spatial hypersurface that ∇_a does in the space-time, we would have to project every single index of the full space-time co-variant derivative as follows,

$$D_a T^b_c = \gamma^d_a \gamma^b_e \gamma^f_c \nabla_d T^e_f, \tag{4.12}$$

now D_a is a spatial tensor that defines the co-variant derivative into each spatial slice of the space-time, and it's compatible with the spatial metric $D_a\gamma_{bc} = 0$, as the co-variant derivative is with the metric $\nabla_a g_{bc} = 0$.

4.2.1 Extrinsic Curvature

At this point, we have to distinguish between the intrinsic curvature coming from the internal space-time structure, defined by the Riemann tensor in terms of the 3-dimensional metric γ_{ab}. And the extrinsic curvature, that comes from the way that the spatial hypersurfaces Σ_t are embedded in the 4-dimensional space-time.

The extrinsic curvature measures the change of the normal vector n^a when it is parallel-transported from one point in Σ_t to another. So the spatial co-variant derivative of n^a,

$$K_{ab} = -\gamma^c_a \gamma^d_b \nabla_c n_d, \tag{4.13}$$

will define this variation. Introducing the expression for the projection operator,

$$\begin{aligned} K_{ab} &= -(g^c_a + n_a n^c)(g^d_b + n_b n^d)\nabla_c n_d, \\ &= -\nabla_a n_b - n_a n^c \nabla_c n_b, \end{aligned} \tag{4.14}$$

where $n^d \nabla_c n_d = 0$ because of the normalization.

Equivalently, the extrinsic curvature can be written as the Lie derivative of the spatial metric along the normal direction. Finding that it can be seen as the velocity of γ_{ab} seen by an Eulerian observer,

$$\begin{aligned}\pounds_{n^a}\gamma_{ab} &= n^c\nabla_c\gamma_{ab} + \gamma_{cb}\nabla_a n^c + \gamma_{ac}\nabla_b n^c, \\ &= n^c\nabla_c(g_{ab} + n_a n_b) + (g_{cb} + n_c n_b)\nabla_a n^c + (g_{ab} + n_a n_c)\nabla_b n^c, \\ &= 2(\nabla_a n_b + n_a n^c \nabla_c n_b), \\ &= -2K_{ab}.\end{aligned} \tag{4.15}$$

So the extrinsic curvature takes the form,

$$K_{ab} = -\frac{1}{2}\pounds_{n^a}\gamma_{ab}. \tag{4.16}$$

4.2.2 Decomposition of the Riemann tensor

We want to relate 4-dimensional ${}^{(4)}R_{abcd}$ to 3-dimensional (R_{abcd},K_{ab}), note the superscript to denote that we refer to a whole space-time quantity. We consider,

$$\begin{aligned}{}^{(4)}R_{abcd} &= g^p_a g^q_b g^r_c g^{s\,(4)}_d R_{pqrs} \\ &= (\gamma^p_a - n_a n^p)(\gamma^q_b - n_b n^q)(\gamma^r_c - n_c n^r)(\gamma^s_d - n_d n^s)^{(4)}R_{pqrs} \\ &= \gamma^p_a\gamma^q_b\gamma^r_c\gamma^{s\,(4)}_d R_{pqrs} + && (4.17)\\ &\quad - \gamma^p_a\gamma^q_b\gamma^r_c n_d n^{s\,(4)}R_{pqrs} + && (4.18)\\ &\quad + \gamma^p_a\gamma^q_b n_c n^r n_d n^{s\,(4)}R_{pqrs} && (4.19)\\ &\quad + \dots,\end{aligned}$$

the other terms would be zero because of the symmetries of R_{abcd}. We see that there are three different projections of the Riemann tensor (4.17, 4.18, 4.19) that would lead to the different equations: *Gauss*, *Codazzi* and *Ricci* equations.

Constraints

Taking equation (4.17) we can define *Gauss'* equation as,

$$\gamma^p_a\gamma^q_b\gamma^r_c\gamma^{s\,(4)}_d R_{pqrs} = R_{abcd} + K_{ac}K_{bd} - K_{ad}K_{cb}, \tag{4.20}$$

that relates the intrinsic curvature of the embedded space to the intrinsic curvature of the embedding space using the extrinsic curvature. If we contract (4.20) with γ^{ac} we get,

$$\gamma^{pr}\gamma^{q}_{b}\gamma^{s\,(4)}_{d}R_{pqrs} = R_{bd} + KK_{bd} - K^{c}_{d}K_{cb}, \tag{4.21}$$

where we have introduced the trace of K_{ab}, $K = \gamma^{ab}K_{ab}$. Now we can contract once more with γ^{bd} and we get,

$$\gamma^{pr}\gamma^{qs\,(4)}R_{pqrs} = R + K^2 - K_{ab}K^{ab}. \tag{4.22}$$

Introducing the definition of γ^{ab} (4.11), and working out the term of the LHS,

$$\gamma^{pr}\gamma^{qs\,(4)}R_{pqrs} = 2n^{p}n^{r}G_{pr}, \tag{4.23}$$

where G_{pr} is the Einstein tensor. So, in terms of the energy density $\rho = n^{p}n^{r}T_{pr}$ we get to the **Hamiltonian constraint**,

$$R + K^2 - K_{ab}K^{ab} = 16\pi\rho. \tag{4.24}$$

We do the same for the projections (4.18), so we define the *Codazzi's* equation that relates the first projection of the Riemann tensor to co-variant derivatives of the extrinsic curvature,

$$\gamma^{p}_{a}\gamma^{q}_{b}\gamma^{r}_{c}n^{s\,(4)}R_{pqrs} = D_{b}K_{ac} - D_{a}K_{bc}, \tag{4.25}$$

similarly, the contractions of *Codazzi* equation leads to the **momentum constraint**,

$$D_{b}K^{b}_{a} - D_{a}K = 8\pi S_{a}, \tag{4.26}$$

where S_a is the momentum density observed by a normal observer, $S_a = -\gamma^{b}_{a}n^{c}T_{bc}$.

Note that equations (4.24, 4.26) don't contain time derivatives, this is the reason why they are called constraints, they must be satisfied all times. The constraints are also independent of the gauge functions α and β^i, a fact that indicates that they refer purely to a given hypersurface.

Evolution equations

Finally we obtain the evolution equations from the projections (4.19) of the 4-dimensional Riemann tensor, that leads to the *Ricci's* equation,

$$n^{d}n^{c}\gamma^{q}_{a}\gamma^{r\,(4)}_{b}R_{drcq} = \pounds_{n^{a}}K_{ab} + \frac{1}{\alpha}D_{a}D_{b}\alpha + K^{c}_{b}K_{ac}, \tag{4.27}$$

introducing the Einstein field equations, *Ricci* equation leads to,

$$\begin{aligned}\pounds_{n^a} K_{ab} = &-\frac{1}{\alpha} D_a D_b \alpha + R_{ab} - 2K_{ac}K^c_b \\ &+ KK_{ab} - 8\pi\left(S_{ab} - \frac{1}{2}\gamma_{ab}(S-\rho)\right),\end{aligned} \tag{4.28}$$

where $S_{ab} = \gamma^c_a \gamma^d_b T_{cd}$ and $S = \gamma^{ab} S_{ab}$. This equation is not a constraint, since the Lie derivative denotes a derivative along the normal (time) direction.

4.3 The York-ADM equations

The commonly known Arnowitt-Deser-Misner (ADM) equations [28], actually non-trivial rewrote by York, are formed by the set of equations (4.16, 4.24, 4.26, 4.28), rewriting the Lie derivative in the form $\pounds_{n^a} = \frac{1}{\alpha}(\pounds_t - \pounds_{\vec{\beta}})$, with $\pounds_t \equiv \partial_t$ and expanding the Lie derivative along the shift vector,

- Constraints

$$R + K^2 - K_{ij}K^{ij} = 16\pi\rho, \tag{4.29}$$

$$D_i(K^{ij} - \gamma^{ij}K) = 8\pi S^i. \tag{4.30}$$

- Evolution

$$\partial_t \gamma_{ij} = -2\alpha K_{ij} + D_i\beta_j + D_j\beta_i, \tag{4.31}$$

$$\begin{aligned}\partial_t K_{ij} = &\alpha(R_{ij} - 2K_{ik}K^k_j + KK_{ij}) \\ &- D_iD_j\alpha - 8\pi\alpha(S_{ij} - \frac{1}{2}\gamma_{ij}(S-\rho)) \\ &+ \beta^k\partial_k K_{ij} + K_{ik}\partial_j\beta^k + K_{kj}\partial_i\beta^k.\end{aligned} \tag{4.32}$$

4.4 The BSSN equations

The set of equations (4.29-4.32) are evolved using a free evolution approach in a numerical simulation, where the constraints equations are solved initially to get proper initial data, then evolve in time solving the evolution equations for γ_{ij} and K_{ij}. However, in numerical relativity, the ADM equations are only weakly hyperbolic, a fact that leads to the lack of the necessary stability properties for long-term numerical simulations.

This problem was solved by Nakamura, Oohara and Kojima [29]. They presented a reformulation of the ADM evolution equations based on a conformal transformation, and Baumgarte and Shapiro showed that this new formulation has far superior stability properties. Known as the BSSN (Baumgarte, Shapiro, Shibata, Nakamura) formulation [30, 31], it is used by most large codes in numerical relativity. This formulation is characterized by introducing a contracted connection term as a new variable, a conformal decomposition of the metric and extrinsic curvature variables, and adding constraints to the evolution equations.

Let's first consider a conformal re-scaling of the spatial metric,

$$\tilde{\gamma_{ij}} = \psi^{-4}\gamma_{ij}, \tag{4.33}$$

where ψ is the conformal factor, chosen in a way that the conformal metric has unit determinant $\det \tilde{\gamma_{ij}} = 1$, condition we ask to be satisfied during the evolution. That implies

$$\psi^4 = \det \gamma_{ij}{}^{1/3}. \tag{4.34}$$

In practice, one works with the logarithm of the conformal factor $\phi = \ln \psi = \frac{1}{12} \ln \det \gamma_{ij}$. An evolution equation for this new variable can be found using equation (4.31),

$$\partial_t \phi = -\frac{1}{6}(\alpha K - \partial_i \beta^i) + \beta^i \partial_i \phi. \tag{4.35}$$

At the same time, in the BSSN formulation, the extrinsic curvature is separated into its trace K and its trace-free part,

$$A_{ij} = K_{ij} - \frac{1}{3}\gamma_{ij} K, \tag{4.36}$$

and a conformal re-scaling of the trace-less extrinsic curvature is also done,

$$\tilde{A}_{ij} = \mathrm{e}^{-4\phi} A_{ij}. \tag{4.37}$$

The BSSN formulation also introduces three new variables known as the conformal connection functions defined as,

$$\tilde{\Gamma}^i = \tilde{\gamma}^{ij}\tilde{\Gamma}^i_{jk} = -\partial_j \tilde{\gamma}^{ij}, \tag{4.38}$$

where $\tilde{\Gamma}^i_{jk}$ is the Cristoffel symbol associated with $\tilde{\gamma}_{ij}$.

Now we have to find evolution equations for these new variables. An evolution equation for ϕ is already found (4.35), and for the rest of the variables they can be obtained from the ADM evolution equations,

$$\frac{d}{dt}\tilde{\gamma}_{ij} = -2\alpha\tilde{A}_{ij}, \tag{4.39}$$

$$\frac{d}{dt}\phi = -\frac{1}{6}\alpha K, \tag{4.40}$$

$$\frac{d}{dt}\tilde{A}_{ij} = \mathrm{e}^{-4\phi}\left(-D_iD_j\alpha + \alpha R_{ij} + 4\pi\alpha[\gamma_{ij}(S-\rho) - 2S_{ij}]\right)^{\mathrm{TF}} + \alpha(K\tilde{A}_{ij} - 2\tilde{A}_{ik}\tilde{A}^k_j), \tag{4.41}$$

$$\frac{d}{dt}K = -D_iD^i\alpha + \alpha\left(\tilde{A}_{ij}\tilde{A}^{ij} + \frac{1}{3}K^2\right) + 4\pi\alpha(\rho + S), \tag{4.42}$$

where $d/dt = \partial_t - \pounds_{\vec{\beta}}$ and TF denotes the trace-free part in the expression inside.

The co-variant derivatives of the lapse function with respect to the physical metric γ_{ij} can be calculated considering the relation of the Cristoffel symbols,

$$\tilde{\Gamma}^k_{ij} = \Gamma^k_{ij} - 2(\delta^k_i\partial_j\phi + \delta^k_j\partial_i\phi - \gamma_{ij}\gamma^{kl}\partial_l\phi). \tag{4.43}$$

The Ricci tensor associated to the physical metric can be separated into two contributions,

$$R_{ij} = \tilde{R}_{ij} + R^{\phi}_{ij}, \tag{4.44}$$

where $\tilde{R}_{ij}$ is computed exactly as R_{ij} but using $\tilde{\gamma}_{ij}$ instead; and R^{ϕ}_{ij} is given by,

$$R^{\phi}_{ij} = 2\tilde{D}_i\tilde{D}_j\phi - 2\tilde{\gamma}_{ij}\tilde{D}^k\tilde{D}_k\phi + 4\tilde{D}_i\phi\tilde{D}_j\phi - 4\tilde{\gamma}_{ij}\tilde{D}^k\tilde{D}_k\phi, \tag{4.45}$$

where $\tilde{D}_i$ is the co-variant derivative associated to the conformal metric.

To get the full set of equations of the BSSN formulations, we still miss an evolution equation for $\tilde{\Gamma}^i$, that can be obtained from equations (4.38) and (4.31), so,

$$\partial_t\tilde{\Gamma}^i = \tilde{\gamma}^{jk}\partial_j\partial_k\beta^i + \frac{1}{3}\tilde{\gamma}^{ij}\partial_j\partial_k\beta^k + \beta^j\partial_j\tilde{\Gamma}^i - \tilde{\Gamma}^j\partial_j\beta^i + \frac{2}{3}\tilde{\Gamma}^i\partial_j\beta^j - 2(\alpha\partial_j\tilde{A}ij + \tilde{A}^{ij}\partial_j\alpha), \tag{4.46}$$

that can be written in a more compact way,

$$\frac{d}{dt}\tilde{\Gamma}^i = \tilde{\gamma}^{ik}\partial_j\partial_k\beta^i + \frac{1}{3}\tilde{\gamma}^{ij}\partial_j\partial_k\beta^k - 2(\alpha\partial_j\tilde{A}^{ij} + \tilde{A}^{ij}\partial_j\alpha). \tag{4.47}$$

But in a numerical evolution, this equation is still unstable. A key step of the BSSN formulation is to use the momentum constraint to fix the instability of this equation. The momentum constraint (4.26) in terms of the new variables takes the form,

$$\partial_j\tilde{A}^{ij} = -\tilde{\Gamma}^i_{jk}\tilde{A}^{jk} - 6\tilde{a}^{ij}\partial_j\phi + \frac{2}{3}\tilde{\gamma}^{ij}\partial_jK + 8\pi\tilde{j}^i, \tag{4.48}$$

where $\tilde{j}^i = \mathrm{e}^{4\phi} j^i$. So, introducing this equation to (4.47) we obtain,

$$\frac{d}{dt}\tilde{\Gamma}^i = \tilde{\gamma}^{jk}\partial_j\partial_k\beta^i + \frac{1}{3}\tilde{\gamma}ij\partial_j\partial_k\beta^k - 2\tilde{A}^{ij}\partial_j\alpha + 2\alpha\left(\tilde{\Gamma}^i_{jk}\tilde{A}^{jk} + 6\tilde{A}^{ij}\partial_j\phi - \frac{2}{3}\tilde{\gamma}^{ij}\partial_j K - 8\pi\tilde{j}^i\right). \tag{4.49}$$

The final system of evolution equations is formed by (4.39-4.42) and (4.49). This are known as the BSSN equations that have a big advantage with respect to the York-ADM [32] equations (4.29-4.32), BSSN equations lead to a well-posed initial value problem. The BSSN equations are the currently most widely used form of Einstein's equations in numerical relativity.

Our aim now, is to stably evolve these equations using the numerical code described in the next chapter. However, in order to do that, well-posedness may not be enough. A good choice for the coordinate conditions is also required, *i.e.*, for the lapse α (4.6) and shift β^i (4.7). Useful choices for these gauge conditions must keep an event horizon of a controled size, so it not grows out of the numerical domain; and to find symmetries. Suitable options for these conditions are: (i) a specific choice of the Bona-Masso family for the lapse; (ii) and a Gamma-freezing condition for the shift.

Chapter 5

Numerical Procedure

The need of evolving numerically the Einstein field equations during the last orbits of a binary black hole coalescence, which fall into the strongly dynamic and non-linear regime of General Relativity, has led to the writing of several numerical codes to simulate such an evolution: BAM [33], Einstein ToolKit [34] which is based on the Cactus framework, LEAN [35]...

In this thesis we will focus on the BAM code, that is an MPI parallelized code that uses the moving puncture method (see Sec. 5.1) to simulate black hole space-times without excision, and moving boxes mesh refinement, via a free evolution approach.

5.1 Initial Data

Before starting with the evolution, we need the initial data to be evolved. The initial data consist in the 3-dimensional metric and the extrinsic curvature (γ_{ij}, K_{ij}) induced on a space-time hypersurface Σ_t, both related by (4.16). This section will be described closely following [33].

One must be especially careful with the description of space-time singularities. As we have already discussed (Chapter 2) the space-time singularities are found where metric components vanish or they diverge. One approach to avoid problems associated with physical singularities is known as the moving puncture method, that is the one used in BAM. Based on modelling each black hole by adopting the Brill-Lindquist wormhole topology. The asymptotically flat end is compactified to a single point r on R^3 which is referred to as puncture. The gauge conditions change the wormhole to a trumpet geometry during the

evolution that allows the black hole singularities to be hidden by the punctures because of the discrete structure of the numerical grid. Another used technique is the excision, where a portion of the space-time inside the event horizon is not evolved. This should not affect the solution because of the properties of the event horizon, no physics inside the horizon can influence the outside of it.

Proper initial data must satisfy the Einstein constraints and give a realistic representation of the physical system under study. The construction of such an initial data consists of a conformal transformation of the spatial metric and a conformal trace-less split of the extrinsic curvature,

$$\gamma_{ij} = \psi_0^4 \tilde{\gamma}_{ij}, \tag{5.1}$$

$$K_{ij} = \psi_0^{-10} \bar{A}_{ij} + \frac{1}{3}\gamma_{ij} K, \tag{5.2}$$

where $\bar{A}_{ij}$ is trace free.

Initially we require a flat metric $\tilde{\gamma}_{ij} = \delta_{ij}$; and the trace of the extrinsic curvature to be null $K = 0$, choice corresponding to a maximal slice, that decouples Hamiltonian from momentum constraints and form a set of equations for $\bar{A}_{ij}$. The simplest solution for these equations is the trivial one $\bar{A}_{ij} = 0$. In addition, in the case of conformal flatness and maximal slice, the momentum constraint takes the simple form of,

$$\partial_j \bar{A}_{ij} = 0, \tag{5.3}$$

and admits the Bowen-York solutions.

The Hamiltonian constraint, in the conformal flatness, $K = 0$ and the Bowen-York solution for (5.3), becomes an elliptic equation for the conformal factor,

$$\tilde{\Delta}\psi_0 + \frac{1}{8} K^{ij} K_{ij} \psi_0^{-7} = 0, \tag{5.4}$$

where $\tilde{\Delta}$ is the Laplace operator associated with the flat metric. This equation is often solved by decomposing the conformal factor into a Brill-Lindquist contribution plus a regular contribution u which is determined by an elliptic equation on R^3 and is C^∞ everywhere except at the punctures where is C^2,

$$\psi_0 = \psi_{BL} + u, \tag{5.5}$$

$$\psi_{BL} = 1 + \sum_{i=1}^{N} \frac{m_i}{2r_i}, \tag{5.6}$$

where we sum over N possible initial black holes, with m_i that parametrizes the mass of each black hole, equal to the total mass only in a Schwarzschild space-time. In the general case, the ADM mass of the ith puncture is given by,

$$M_i = m_i \left(1 + u_i + \sum_{i \neq j} \frac{m_j}{2d_{ij}} \right), \tag{5.7}$$

where u_i is the value of u at the ith puncture, and d_{ij} is the coordinate distance between the punctures. This quantity agrees within numerical uncertainty with the apparent horizon mass $M_{AH,i}$ for non-spinning punctures; in the case of spinning punctures it agrees with the black hole mass given by the Christodoulou formula,

$$M_i^2 = M_{AH,i}^2 + \frac{S_i^2}{4M_{AH.i}^2}. \tag{5.8}$$

The ingredients left to complete the initial data are the values of the gauge quantities in the spatial hypersurface Σ_t when $t = 0$. Choices for the lapse function and the shift vector that have been successfully used are,

$$\alpha = 1 \qquad \text{or} \qquad \alpha = \psi_0^{-2}, \tag{5.9}$$

$$\beta^i = 0, \tag{5.10}$$

both to be updated at every time-step following the evolution equations.

5.2 Evolution

To evolve the described initial data with the evolution equations due to BSSN formalism, first we have to relate the variables in the conformal transverse-trace-less decomposition with the BSSN variables. On the initial slice they are related by,

$$\phi = \ln\psi_0, \tag{5.11}$$

$$\tilde{A}_{ij} = \psi^{-6} \bar{A}_{ij}, \tag{5.12}$$

$$\tilde{\Gamma}^i = -\partial_j \tilde{\gamma}^{ij}, \tag{5.13}$$

and γ_{ij} and K remain unchanged. Once we have the description of the BSSN variables in the initial spatial hypersurface, these variables are evolved according to the BSSN evolution

equations,

$$\frac{d}{dt}\tilde{\gamma}_{ij} = -2\alpha\tilde{A}_{ij}, \tag{5.14}$$

$$\frac{d}{dt}\phi = -\frac{1}{6}\alpha K, \tag{5.15}$$

$$\frac{d}{dt}\tilde{A}_{ij} = \mathrm{e}^{-4\phi}(-D_iD_j\alpha + \alpha R_{ij})^{TF} + \alpha(K\tilde{A}_{ij} - 2\tilde{A}_{ik}\tilde{A}^k_j), \tag{5.16}$$

$$\frac{d}{dt}K = -D_iD^i\alpha + \alpha\left(\tilde{A}_{ij}\tilde{A}^{ij} + \frac{1}{3}K^2\right), \tag{5.17}$$

$$\begin{aligned}\frac{d}{dt}\tilde{\Gamma}^i = {} & \tilde{\gamma}^{jk}\partial_j\partial_k\beta^i + \frac{1}{3}\tilde{\gamma}ij\partial_j\partial_k\beta^k - 2\tilde{A}^{ij}\partial_j\alpha \\ & + 2\alpha\left(\tilde{\Gamma}^i_{jk}\tilde{A}^{jk} + 6\tilde{A}^{ij}\partial_j\phi - \frac{2}{3}\tilde{\gamma}^{ij}\partial_j K\right),\end{aligned} \tag{5.18}$$

where matter terms have been set to zero. The Lie derivatives with respect tensor quantities that appear in $d/dt = \partial_t - \pounds_{\vec{\beta}}$ are given by,

$$\pounds_{\vec{\beta}}\phi = \beta^k\partial_k\phi + \frac{1}{6}\partial_k\beta^k, \tag{5.19}$$

$$\pounds_{\vec{\beta}}\tilde{\gamma}_{ij} = \tilde{\gamma}_{ij}\partial_k\tilde{\gamma}_{ij} + \tilde{\gamma}_{ik}\partial_j\beta^k + \tilde{\gamma}_{jk}\partial_i\beta^k - \frac{2}{3}\tilde{\gamma}_{ij}\partial_k\beta^k, \tag{5.20}$$

$$\pounds_{\vec{\beta}}\tilde{A}_{ij} = \tilde{A}_{ij}\partial_k\tilde{A}_{ij} + \tilde{A}_{ik}\partial_j\beta^k + \tilde{A}_{jk}\partial_i\beta^k - \frac{2}{3}\tilde{A}_{ij}\partial_k\beta^k. \tag{5.21}$$

To improve the stability of the simulation, is a common practice to evolve the BSSN evolution system as a partially constrained system, enforcing the algebraic constraints $\det(\gamma_{ij}) = 1$ and $\mathrm{Tr}(\tilde{A}_{ij}) = 0$ at every full or intermediate step. Moreover, the algebraic constraints and the first order differential constraint $\tilde{\Gamma}^i = -\partial_j\tilde{\gamma}^{ij}$ can be used for the source terms without affecting well-posedness. Translated to the BAM code:

- Explicitly use $\tilde{\Gamma}^i = -\partial_j\tilde{\gamma}^{ij}$ instead of the evolved variable $\tilde{\Gamma}^i$ whenever it appears undifferentiated.
- Algebraic constraints are imposed when the right-hand sides are computed and at the end of each evolution step.

5.2.1 Conformal factor

In the moving punctures approach, the wormhole topology of the space-time is captured by th conformal factor, that diverges at each puncture $\psi \sim 1/r$. The singularity in the

numerical grid is avoided due to the choice of the gauge. In order to evolve the divergent conformal factor two methods have been found to work: the ϕ-method and the χ-method.

In the ϕ-method our choice of the conformal factor is directly the original BSSN variable ϕ,

$$\phi = \ln\psi, \tag{5.22}$$

so the evolution system remains the same.

In the χ-method a new finite conformal factor at the puncture is defined as,

$$\chi = \psi^{-4}, \tag{5.23}$$

and a new evolution equation has to be found to replace (5.15),

$$\frac{d}{dt}\chi = \frac{2}{3}\chi(\alpha K - \partial_j \beta^j). \tag{5.24}$$

5.2.2 Gauge conditions

The gauge conditions (α, β^i) in both ADM and BSSN evolution systems are freely specifiable. To describe the gauge conditions we have to keep in mind that the choice of them will allow us to avoid the singularity in the numerical grid. In order to achieve that, we let the lapse function and the shift vector to change in time in such a way that the evolution in proper time should be slowed down in regions where hypersurfaces approach a singularity. In the moving puncture method, the standard choice for evolving the lapse function in the BSSN formalism is given by the co-variant form of "1+log" slicing,

$$(\partial_t - \beta^i \partial_i)\alpha = -2\alpha K. \tag{5.25}$$

Suitable choices for the shift vector in order to obtain long term stable numerical simulations is evolve β^i according to a Gamma-freezing condition,

$$\partial_t \beta^i = \frac{3}{4} B^i, \tag{5.26}$$

$$\partial_t B^i = \partial_t \tilde{\Gamma}^i - \eta B^i. \tag{5.27}$$

5.3 Numerical Method

To produce the binary black hole simulation we will use the BAM code, whose features focus on the already mentioned moving punctures method to simulate black hole spacetimes without excision and uses the moving boxes mesh refinement.

5.3.1 Evolution Method

To evolve the produced initial data we need two basic ingredients: the evolution system, that we have already described and it leads to the set of the BSSN evolution equations (5.14-5.18); and the discretization algorithm, allowing us to discretize the spatial domain [36]. A suitable numerical algorithm is needed to satisfy the well-posedness of the system.

Method of Lines: The BAM code uses the method of lines approach to separate the time and space discretization process. The equations in the *3+1* form are evolved in time using a Runge-Kutta algorithm while the spatial right hand side can be separately discretized. Here a finite difference scheme is used.

Artificial Dissipation: In order to avoid high frequency noise from mesh refinement boundaries artificial dissipation terms have been included in the RK4 evolution, even if they are not required for stability. Dissipation terms can be included in the form,

$$\partial_t u \rightarrow \partial_t u + Qu, \tag{5.28}$$

where Q is the Kreiss-Oliger dissipation operator,

$$Q = \sigma(-h)^{2r-1}(D_+)^r \rho (D_-)^r / 2^{2r}, \tag{5.29}$$

for a $(2r-2)$ resolution. Here σ is a parameter to control the effect of the dissipation terms, and ρ is a weight function currently set to unity.

5.3.2 Adaptive Mesh Refinement

Black hole space-times involve a wide range of length scales which cannot be efficiently accommodated inside uniform grids and thus require the use of mesh refinement, *i.e.* a grid resolution that varies in space and time [37]. In the BAM code, a Berger-Oliger type adaptive mesh refinement is implemented [38].

The computational domain consists of a set of nested boxes centered around the individual black holes immersed inside more large boxes containing both black holes. In practice, there are L different levels of refinement, each labeled by $l = 0, \ldots, L-1$. One specific level l consists in a Cartesian grid with constant grid spacing h_l. Each grid is completely contained in the next outer level, with grid spacing that differs from the previous

one by a factor of 2. So labelling the outermost level with $l = 0$, with a grid resolution h_0, the resolution at the following levels are $h_l = h_0/2^l$, until the innermost level $L - 1$.

In the case of a binary black hole, when the two punctures are far enough, the hierarchy of the refinement levels consists in non overlapping grids centered in each black hole, boxes in 3D. The size of each box is given by $h_l \times N_l$, where h_l is the resolution of the level l, and N_l is the number of discrete points in that level. When the boxes of both black holes overlap, they are replaced by their bounding box, the smallest rectangular box that contains the two original boxes.

The hierarchy of the boxes evolves as the puncture moves. The position of a puncture is tracked using the Crank-Nicholson method by integrating [39],

$$\partial_t x^i_{punc} = -\beta^i(x^i_{punc}). \tag{5.30}$$

The outermost level $L = 0$ and some of the following finer levels are boxes with a fixed size centered at the origin to avoid unnecessary grid motion.

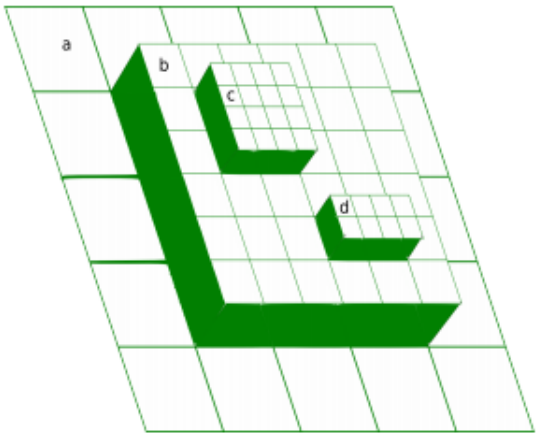

Figure 5.1: Example of a two dimensional domain. Three different levels are shown. The two boxes fixed of resolution h_0 and h_1 are labeled by "a" and "b"; and the two boxes "c" and "d" of resolution h_2 would represent the moving boxes around each black hole. Source: [40].

5.3.3 Extraction quantities

In each spatial hypersurface, physical information about the binary black hole simulation is extracted. To have a good notion of the quality of the simulation a key step is a

good understanding of the results rather than solving the two body problem itself. Some diagnostics quantities and how does BAM compute them is described here.

Gravitational Waves: The difference between the Newtonian theory and General Relativity in the two body problem is that in GR the system radiates energy in the form of gravitational waves. The most commonly used approach to extract gravitational waves from black hole binaries simulations is the Newman-Penrose formalism. A description of how the BAM code computes the waveforms as well as the radiated momenta and energy from the knowledge of γ_{ij} and K_{ij} of Σ_t is provided.

The Newman-Penrose scalar is defined as,

$$\Psi_4 = -{}^{(4)}R_{abcd} n^a \bar{m}^b n^c \bar{m}^d, \tag{5.31}$$

where R_{abcd} is the Riemann tensor of the 4-dimensional space-time; n and $\bar{m}$ form part of a null-tetrad $l, n, m, \bar{m}$ where l and n denote ingoing and outgoing null-vectors. The complex value $\bar{m}$ is constructed out of two spatial vectors orthogonal to l and n such that,

$$-l \cdot n = m \cdot \bar{m} = 1, \tag{5.32}$$

with all other inner products between 4-vectors vanishing. The tetrad vector are given by,

$$n^0 = \frac{1}{\sqrt{2}\alpha} \qquad n^i = \frac{1}{\sqrt{2}} \left(\frac{-\beta^i}{\alpha} - v^i \right), \tag{5.33}$$

$$l^0 = \frac{1}{\sqrt{2}\alpha} \qquad l^i = \frac{1}{\sqrt{2}} \left(\frac{-\beta^i}{\alpha} + v^i \right), \tag{5.34}$$

$$m^0 = 0 \qquad m^i = \frac{1}{\sqrt{2}} \left(u^i + i w^i \right), \tag{5.35}$$

where n^a is the normal vector to the spatial hypersurface; and (u^i, v^i, w^i) form an orthonormal spatial basis constructed using the Gram-Schmidt method, that in Cartesian coordinates take the form,

$$u^i = (-x, y, 0), \tag{5.36}$$

$$v^i = (x, y, z), \tag{5.37}$$

$$w^i = g^{ia} \epsilon_{abc} u^b v^c. \tag{5.38}$$

In order to compute the Newman-Penrose scalar in a spatial hypersurface, we need to express it in terms of 3-dimensional quantities in that hypersurface and the spatial

vectors described above. We project the 4-dimensional Riemann tensor to get the following relations, associated to *Gauss* and *Codazzi* equations (4.20,4.25),

$$\gamma_a^p\gamma_b^q\gamma_c^r\gamma_d^{s(4)}R_{pqrs} = R_{abcd} + K_{ac}K_{bd} - K_{ad}K_{cb}, \tag{5.39}$$

$$\gamma_a^p\gamma_b^q\gamma_c^r n^{s(4)}R_{pqrs} = D_bK_{ac} - D_aK_{bc}, \tag{5.40}$$

$$\gamma^{pr}\gamma_b^q\gamma_d^{s(4)}R_{pqrs} = R_{bd} + KK_{bd} - K_d^cK_{cb}, \tag{5.41}$$

here we have used the projection operator defined as (4.11). So the Newman-Penrose scalar takes the form,

$$\Psi_4 = -\frac{1}{4}\left({}^{(4)}R_{abcd}v^av^c - 2\gamma_a^p\gamma_b^q\gamma_c^r n^{s(4)}R_{pqrs}v^c + \gamma^{pr}\gamma_b^q\gamma_d^{s(4)}R_{pqrs}\right)(u^b - iw^b)(u^d - iw^d). \tag{5.42}$$

We can project Ψ_4 onto spherical harmonics Y^s_{lm} defined in terms of Wigner d-functions [41] of spin weight -2, obtaining the contribution of the individual modes l, m,

$$A_{lm} = \langle Y^{-2}_{lm}, \Psi_4\rangle = \int_0^{2\pi}\int_0^{\pi}\Psi_4\overline{Y^{-2}_{lm}}\sin\theta d\theta d\phi. \tag{5.43}$$

In principle gravitational wave extraction has to be done at infinity, but in practice the right hand side of (5.43) is evaluated on the Cartesian grid and interpolated onto a sphere of finite extraction radius r_{ext} using fifth-order polynomials. The integration over the sphere is performed using the fourth-order Simpson method.

However, to reduce computational costs, the symmetry properties of the space-time have to be used. This way, for $s = -2$ and $l = m = 2$, we can rewrite equation (5.43) as,

$$A_{22} = \langle Y^{-2}_{22}, \Psi_4\rangle = \int_0^{2\pi}\int_0^{\pi/2}\left(\Psi_4\overline{Y^{-2}_{22}} + \overline{\Psi_4}Y^{-2}_{22}\right)\sin\theta d\theta d\phi. \tag{5.44}$$

It is important to remark that most of the energy is radiated in the $l = 2$ and $|m| = 2$ modes.

Often one may be interested in the energy and momenta radiated away in the form of gravitational waves, in terms of the Newman-Penrose scalar we can write them as,

$$\frac{dE}{dt} = \lim_{r\to\infty}\left[\frac{r^2}{16\pi}\int_\Omega\left|\int_{-\infty}^t\Psi_4 d\tilde{t}\right|^2 d\Omega\right], \tag{5.45}$$

$$\frac{dP_i}{dt} = -\lim_{r\to\infty}\left[\frac{r^2}{16\pi}\int_\Omega l_i\left|\int_{-\infty}^t\Psi_4 d\tilde{t}\right|^2 d\Omega\right], \tag{5.46}$$

$$\frac{dJ_z}{dt} = -\lim_{r\to\infty}\left\{\frac{r^2}{16\pi}\mathrm{Re}\left[\int_\Omega\left(\partial_\phi\int_{-\infty}^t\Psi_4 d\tilde{t}\right)\left(\int_{-\infty}^t\int_{-\infty}^{\hat{t}}\overline{\Psi_4}d\tilde{t}d\hat{t}\right)d\Omega\right]\right\}, \tag{5.47}$$

where $l_i = (-\sin\theta\cos\phi, -\sin\theta\sin\phi, -\cos\phi)$. Equation (5.45) can be also written in terms of (5.43) as,

$$\frac{dE}{dt} = \lim_{r\to\infty}\left[\frac{r^2}{16\pi}\left|\int_{-\infty}^{t}\sum_{l,m}A_{lm}d\tilde{t}\right|^2\right]. \tag{5.48}$$

Horizons: A key feature that defines a black hole is its event horizon, a region in the space-time that separate the points from which null geodesics can reach the space-time and points from which they cannot [37]. However, to define the event horizon one needs to know the entire history of the space-time. A more convenient definition is used, and that's the one of apparent horizon. We can define it as the outermost marginally trapped surface on a spatial slice Σ_t, it is defined locally in time in a space-like slice and depends only on data in that slice. Numerical algorithms to compute apparent horizons have been developed [42], as solution of elliptic PDE.

Global quantities: For asymptotically flat space-times, the expression for the energy-momentum at spatial infinity was given by Arnowitt, Deser and Misner in their Hamiltonian formalism [43]. The expressions can be given as limits of surface integrals defined at finite radius, the surfaces are taken as spheres S_r of radius r. These surface integrals take the form,

$$E(r) = \frac{1}{16\pi}\int_{S_r}\sqrt{\gamma}\gamma^{ij}\gamma^{kl}(\gamma_{ik,l} - \gamma_{ij,k})\,dS_l, \tag{5.49}$$

$$P_j(r) = \frac{1}{8\pi}\int_{S_r}\sqrt{\gamma}(K^i_j - \delta^i_j K)\,dS_i, \tag{5.50}$$

$$J_j(r) = \frac{1}{8\pi}\epsilon^m_{jl}\int_{S_r}\sqrt{\gamma}x^l(K^i_m - K\delta^i_m)\,dS_i, \tag{5.51}$$

in terms of the 3-dimensional induced metric γ_{ij} and the extrinsic curvature K_{ij}. Then the ADM energy M_{ADM} and the linear and angular momentum are given as the limit of (5.49-5.51),

$$M_{ADM} = \lim_{r\to\infty} E(r), \tag{5.52}$$

$$P_j = \lim_{r\to\infty} P_j(r), \tag{5.53}$$

$$J_j = \lim_{r\to\infty} J_j(r), \tag{5.54}$$

and the rest mass can be defined as $M_R^2 = M_{ADM}^2 - \sum_{j=1,3} P_j P_j$.

5.4 Wave equation as a Toy Model for Hyperbolic Equations

To get a feeling of how the evolution code works, let's consider a similar case to the Einstein's field equations but simpler: the wave equation. Going through the wave equation in 1+1 dimensions (one spatial dimension + time), will allow us to explore various useful concepts in numerical simulations such as finite difference, characteristic analysis, the Method of Lines for evolving hyperbolic PDE's, the Courant-Friedrichs-Lewy stability criterion and convergence testing [44, 45].

Let's start with the wave equation,

$$\Box\phi = -\frac{\partial^2\phi}{\partial t^2} + \frac{\partial^2\phi}{\partial x^2} = 0, \tag{5.55}$$

with $\Box\phi$ being the flat space D'Alembertian operator applied to ϕ; and working in units where $c = 1$. Performing a complete first order reduction we get to the set of evolution equations,

$$\partial_t\pi = \partial_x(\psi + \beta\pi), \tag{5.56}$$

$$\partial_t\psi = \partial_x(\pi + \beta\psi), \tag{5.57}$$

$$\partial_t\phi = \pi + \beta\psi, \tag{5.58}$$

where β is the shift vector but in 1D, and the functions π and ψ are defined by,

$$\pi = \partial_t\phi - \beta\partial_x\phi, \tag{5.59}$$

$$\psi = \partial_x\phi. \tag{5.60}$$

The wave equation is completely described by equations (5.56) and (5.57), that can be numerically integrated together with (5.58) to get the physical variable ϕ.

Characteristic analysis: We can rewrite equations (5.56) and (5.57) as an evolution system for a vector such as,

$$\partial_t\mathbf{u} + \mathbf{A}\partial_x\mathbf{u} = \mathbf{u}\partial_x\beta, \tag{5.61}$$

where $\mathbf{u} = (\pi, \psi)^T$, and

$$\mathbf{A} = -\begin{pmatrix} \beta & 1 \\ 1 & \beta \end{pmatrix}, \tag{5.62}$$

whose eigenvalues are

$$\lambda_1 = -\beta + 1, \tag{5.63}$$

$$\lambda_2 = -\beta - 1, \tag{5.64}$$

which are distinct and real, corresponding to a strictly hyperbolic system; and has the characteristic variables given by its eigenvectors

$$\mathbf{w} = \frac{1}{2}(\pi - \psi, \pi + \psi)^T, \tag{5.65}$$

corresponding to the right going and left going modes of the scalar field.

Initial Data: To provide initial data for $\pi(0, x)$ and $\psi(0, x)$ is equivalent to say that we provide intial data for $\phi(0, x)$ and $\partial_t(\phi(0, x))$ in the second order system. The initial data for $\phi(0, x)$ is freely specifiable, in our case we will consider a Gaussian,

$$\phi(0, x) = A\mathrm{e}^{-\frac{(x-x_0)^2}{\sigma^2}}, \tag{5.66}$$

then, the initial data for π and ψ comes from the time and spatial derivatives of ϕ. For $\pi(0, x)$, we will require $\pi(0, x) = 0$ for time-symmetric initial data. For $\psi(0, x)$, we just use the equation (5.60),

$$\pi(0, x) = 0, \tag{5.67}$$

$$\psi(0, x) = -2\frac{(x - x_0)}{\sigma^2}\phi(0, x). \tag{5.68}$$

Boundary Conditions: Periodic, reflection and outgoing boundary conditions have been implemented and tested. Here we will focus on the last ones since they represent the physical situation better, the initial pulse propagates outside our numerical domain once it reaches its boundaries. To code these radiative boundary conditions we have to set that there is no incoming waves at the boundary. In order to do that, we set to zero the right going mode at the left boundary and the equivalent at the right one.

Numerical Algorithm: To evolve such an hyperbolic system, the Method of Lines is used. It consist in discretizing the spatial dimension, using a finite difference scheme, and integrate in time using a Runge-Kutta method. The set of equations to evolve (5.56-5.58) are all of the type

$$\partial_t f = S(f), \tag{5.69}$$

where $S(f)$ is a spatial operator applied to f. To discretize the spatial right hand side a equispaced numerical grid is defined, dividing the continuous domain into J discrete points labeled by $i = 1, \ldots, J$; so the discrete domain is now $x_i = i\Delta x$. The spatial derivative is given by its centered finite difference schemes, which at second or fourth order are,

$$\partial_x f = \frac{f_{i+1} - f_{i-1}}{2\Delta x} + \mathcal{O}(\Delta x^2), \tag{5.70}$$

$$\partial_x f = \frac{-f_{i+2} + 8f_{i+1} - 8f_{i-1} + f_{i-2}}{12\Delta x} + \mathcal{O}(\Delta x^4), \tag{5.71}$$

respectively. A fourth order Runge-Kutta method is used to integrate the right hand side in time,

$$\begin{aligned}
k_1 &= S(t^{n-1}, f^{n-1}), \\
k_2 &= S(t^{n-1} + \frac{\Delta t}{2}, f^{n-1} + \frac{\Delta t}{2} k_1), \\
k_3 &= S(t^{n-1} + \frac{\Delta t}{2}, f^{n-1} + \frac{\Delta t}{2} k_2), \\
k_4 &= S(t^{n-1} + \Delta t, f^{n-1} + \Delta t k_3), \\
f^n &= f^{n-1} + \frac{\Delta t}{6}(k_1 + 2k_2 + 2k_3 + k_4),
\end{aligned} \tag{5.72}$$

where f^{n-1} denotes the function to integrate at the previous time step t^{n-1}, and f^n is the integrated function at the new time step t^n.

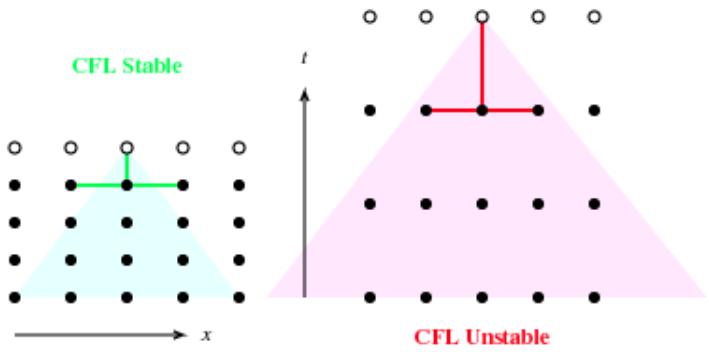

Figure 5.2: Visualization of the CFL condition, shaded regions represent physical domain of influence while discrete points represent numerical domain. A spatial three-points centered finite difference scheme for the evolution is shown. Source: http://www.physics.buffalo.edu/phy410-505/2011/topic3/app2/index.html.

Courant-Friedrichs-Lewy Factor: Is a stability condition named after Richard Courant, Kurt Friedrichs and Hans Lewy [46], required to solve partial differential equations with the Method of Lines. It is a relation between the time step and the spatial step of the form,

$$C_{max} \geq \frac{c\Delta t}{\Delta x}, \tag{5.73}$$

where c is the magnitude of the velocity previously set to unity. The physical domain at a time t^n that influences the next time step t^{n+1} during the evolution, must be entirely contained in the discretized numerical domain, see Figure 5.2

To evolve the initial Gaussian distribution, the spatial domain was chosen to be $[-1, 1]$ with a $\Delta x = 0.005$. The parameters of the initial Gaussian were $A = 0.01$, $\sigma = 0.1$ and $x_0 = 0$. Different choices of β and the Courant-Friedrichs-Lewy factor were made.

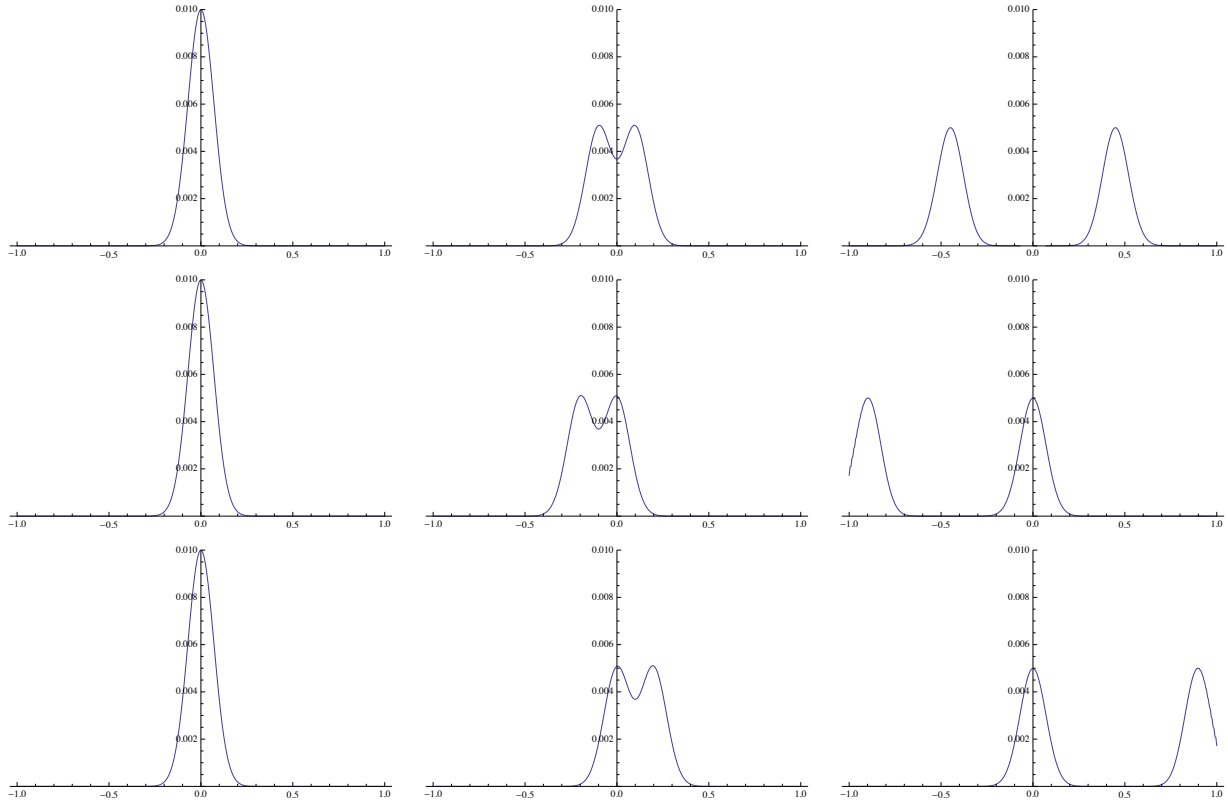

Figure 5.3: Snapshots of the evolution of the initial Gaussian at different time steps. Different choices of the coordinate system corresponding to different β are shown. We use radiative boundary conditions, the wave propagates out of the domain as it reaches the boundary.

As already discussed in Chapter 4, the choice of the gauge quantity β determines our

choice of coordinates. In this case, since we are evolving the wave equation in just one spatial dimension, we have set $\beta = [0, 1, -1]$ to see how different frames are chosen, see Figure 5.3. With the value of $\beta = 0$, the reference frame is fixed in the middle of the numerical domain, set to $[-1, 1]$; but with the values of $\beta = -1, 1$, that corresponds to the speed of light, the reference frame is co-moving with the wave that propagates to the left and to the right respectively. Later, in the code where the Einstein field equations are solved, a suitable choice for this quantity would allow us to freeze the horizon of the black hole in place.

To converge to a stable solution, the Courant-Friedrichs-Lewy factor can be derived analytically as $C_{max} = \sqrt{8}$ [46]. Evolving the wave equation with C larger than C_{max} will lead to high frequency numerical instabilities that grow faster with higher resolution, they appear in the code as shown in Figure 5.4.

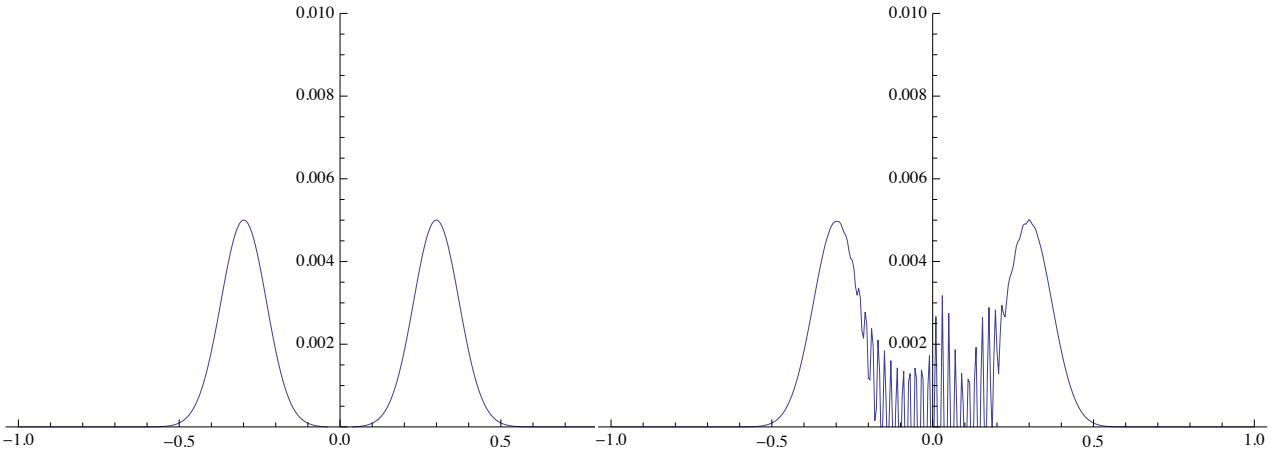

(a) CFL ≤ C_{max} *(b) CFL ≥ C_{max}*

Figure 5.4: Snapshots of the evolution of the initial Gaussian at a certain value of t. If the Courant-Friedrichs-Lewy condition (5.73) is not fulfilled, instabilities in the solution appear.

Moreover, it will be useful to perform a convergence test over the found solution to check the validity and accuracy of the solution. In this case, where both the time integrator and the finite difference stencil for the spatial derivative, is fourth order, we expect a fourth order convergence. To check that, we evaluate differences between the solution computed at different resolutions (see Sec. 6.1.1 for a detailed explanation). One have to take care of evaluate the solution in the different resolutions at the same point in the domain. In Figure 5.5, we see that the differences agree with fourth order convergence.

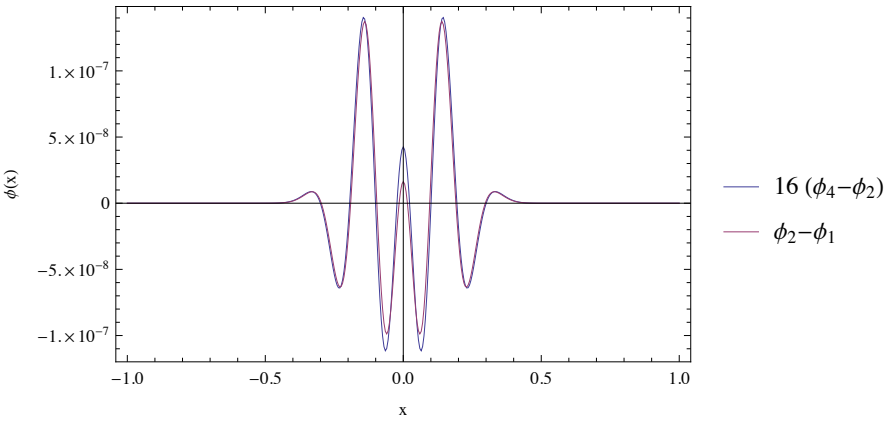

Figure 5.5: Convergence results for the wave equation after 10 *temporal iterations. Solution shows fourth order convergence.*

To evolve the Einstein field equations in the BSSN form, we have to take into account the considerations mentioned above. The evolution will be performed with the BAM code in the next section.

Chapter 6

Numerical Simulations of a Precessing $q = 1.2$ Black Hole Binary

The role of Numerical Relativity begins after the binary has gone through a slow inspiral phase modeled by analytical approximations such as the effective one-body approach. When the fully general relativistic numerical evolution starts, the initial inspiral stage took care of reducing the eccentricity of the orbits via the emission of gravitational waves. The integration of the post-Newtonian equations of motion in the effective one-body form in done over hundreds of orbits from an initial large separation until the binary reaches such separation that only a few orbits remain to the merger. The reason to start the integration of the PN equations from this large separation is to let the radiation reaction circularize the orbits [47].

In this case, we study a $q = M_2/M_1 = 1.2$ [10] binary system, where M_1 and M_2 are the black hole individual masses (see Figure 6.1). The integration of the Post-Newtonian equations is done from an initial separation of $r = 40M$, where $M = M_1 + M_2$; note that both distance and time are scaled with the total mass M. We use Mathematica [48] to evolve during a time of approximately $224\,158M$. In this time, the binary completes around 455 orbits and reaches a separation of $r = 10.62M$. This will be the starting point for the simulation code to accurately simulate the last 5 orbits; the merger, which is estimated to occur after around $1200M$; the ringdown of the system and the gravitational waves emitted.

Opposed to the mass distribution, the spin distribution shows that the spin components are poorly constrained, see Figure 6.2. Specifically, the component that is responsible of

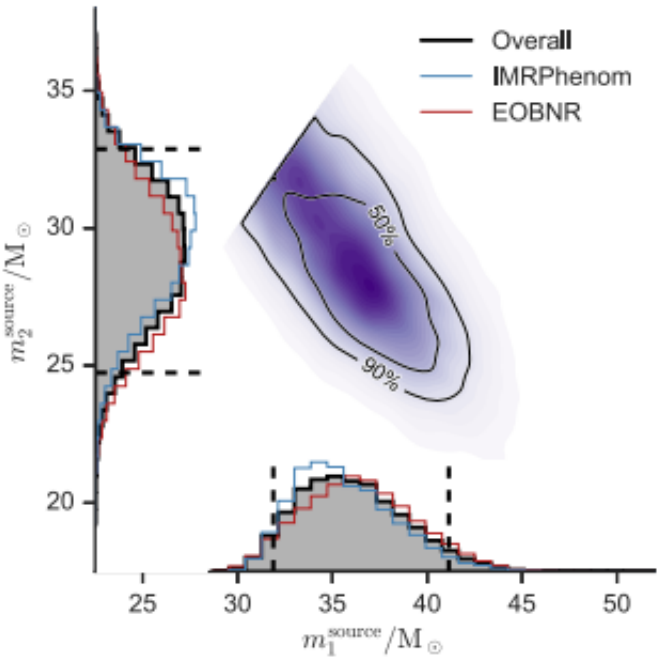

Figure 6.1: Probability distributions for the masses M_1 and M_2 for the individual black holes. Source: [10]

the precession χ_p, is compatible with $\chi_p = 0$ but also with $\chi_p \approx 1$. In this thesis, we choose a precessing configuration (Table 6.1) to show that it is also consistent with GW150914, χ_p is taken to be $\chi_p \approx 0.2$

6.1 Runs Configuration

The simulations were carried out in the BSC-CNS Marenostrum supercomputer [49] using the BAM code. The BSC-CNS Marenostrum is a supercomputer with a peak performance of 1.1 Petaflops; it consists in 2880 nodes with 16 cores per node of 2Gb/core of RAM memory, and 256 nodes with also 16 cores per node of higher memory cores.

As stated, the starting point will be where the integration of the PN equations finishes. There, parameters of the punctures, which define the initial black holes, are summed up in Table 6.1.

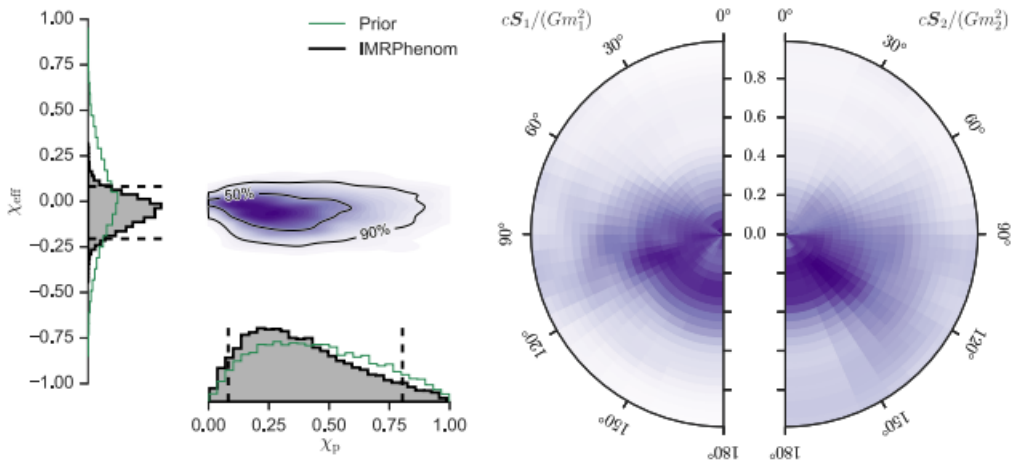

Figure 6.2: Left: Probability distributions for χ_{eff} (component parallel to the orbital angular momentum) and χ_p (component in the orbital plane, responsible of the precession) spin parameters. Right: Probability distributions for the dimensionless spin components relative to the normal to the orbital plane $\boldsymbol{L}$. Source: [10]

$m_1 \approx 0.524$	$x_1 = 0$	$p_{x_1} \approx 0.092$	$s_{x_1} \approx 0.003$
	$y_1 \approx -4.829$	$p_{y_1} \approx 0$	$s_{y_1} \approx 0.033$
	$z_1 = 0$	$p_{z_1} \approx 0.003$	$s_{z_1} \approx 0.023$
$m_2 \approx 0.434$	$x_2 = 0$	$p_{x_2} \approx -0.092$	$s_{x_2} \approx -0.007$
	$y_2 \approx 5.795$	$p_{y_2} \approx 0$	$s_{y_2} \approx -0.035$
	$z_2 = 0$	$p_{z_2} \approx -0.003$	$s_{z_2} \approx -0.021$

Table 6.1: Initial parameters for the numerical Relativity simulation.

The mass of the punctures can be estimated from (5.7), and their values are $M_1 \approx 0.5454$ and $M_2 \approx 0.4545$ with a total ADM mass of $M_{ADM} \approx 0.9903$. This is the set of data required to start the simulation.

Another key step to start the simulation is to define the numerical domain over which we will perform the simulation. As already mentioned, the numerical domain consists of a set of boxes centered around the individual black holes, each one with N_l^3 grid points. Defining a grid spacing for the outermost level h_0 the resolution for the following levels is fixed to be $h_l = h_0/2^l$, with l being the label of each level. For this case, $L = 13$ levels of refinement, labeled by $l = 0, \ldots, 12$, were chosen for both black holes since their horizons'

size are similar. Also, three different simulations with three different resolutions were run in order to perform a convergence test. Table 6.2 shows the different runs with different resolutions (labeled by R_0, R_1 and R_2), the number of points used in each refinement level and the grid spacing of the coarsest level. The number of points in each resolution were consistently rescaled by a factor of 1.25 between the mid and lower resolution, and 1.2 between the high and mid resolution.

Resolution	h_0	Refinement level												
		0	1	2	3	4	5	6	7	8	9	10	11	12
R_0	75	80	80	96	128	160	192	240	240	64	64	64	64	64
R_1	60	100	100	120	160	200	240	300	300	80	80	80	80	80
R_2	50	120	120	144	192	240	288	360	360	96	96	96	96	96

Table 6.2: Resolution of the coarsest level for each run and the number of points in each direction for the different refinement levels.

The two lower resolution runs where carried out in 256 of the 2Gb/core of RAM memory nodes; while the higher resolution run, because of its memory requirements, was carried out in 96 of the 8Gb/core nodes. In the Table 6.3, the time (in CPU hours) and the memory (in Gb) required by each run is specified.

Run	Time (in CPU hours)	Total Memory (in Gb)
R_0	24832	265.9
R_1	36352	381.7
R_2	36384	386.9

Table 6.3: Consumption of each job in terms of time and memory.

Theoretically, the CPU hours should scale by the same factor than the number of points in each resolution does. However, in these runs, in order to save time the lower and mid resolution where run in a high number of nodes, so we lose efficiency because of the parallelization. Between the higher and the other resolutions, the scaling is not the same because the number of nodes used are not the same.

6.1.1 Convergence Test

Once the equations have been solved, we need to perform a convergence test to check both the validity and the accuracy of the solution, and to determine the errors.

The reason why we run the same simulation over three different resolution is because we need to compute the ratio between the differences among the resolutions. Focusing in both Figure 6.3 and Figure 6.4 we appreciate no differences between the three resolutions, but a deeper study of the convergence is required.

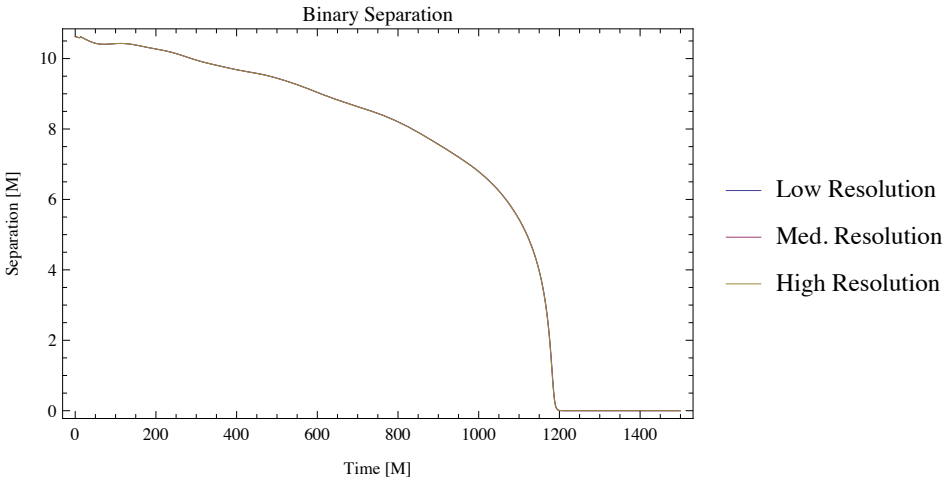

Figure 6.3: Orbital separation as a function of time.

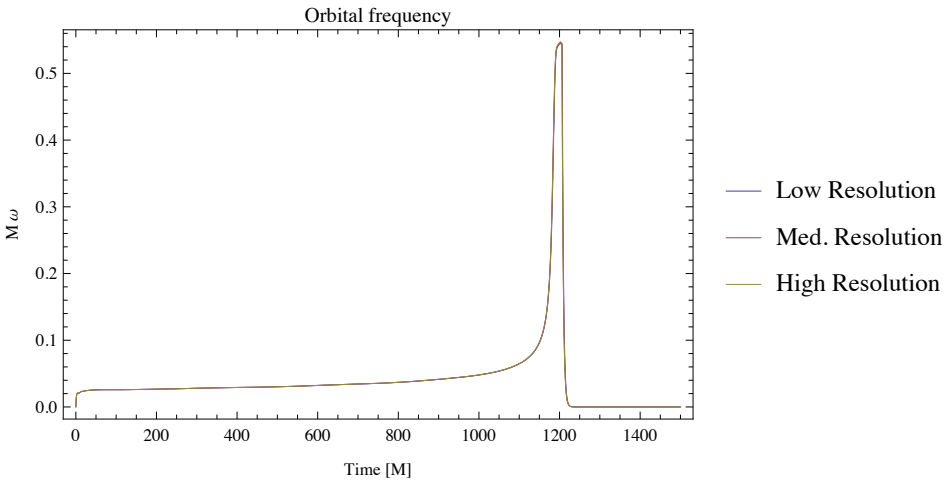

Figure 6.4: Orbital frequency as a function of time.

To make a convergence test, when the solution is not known *a priori*, we compute

the solution for three different integration resolutions $\{\Delta x_0, \Delta x_1, \Delta x_2\}$, with Δx_i the grid spacing in the run R_i. Then, writing the solution obtained as,

$$R_i = R_{exact} + \epsilon(\Delta x_i)^p + \mathcal{O}(\Delta x_i^{p+1}), \tag{6.1}$$

where ϵ is our error. Therefore, computing the ratio between

$$\frac{R_1 - R_0}{R_2 - R_1} = \frac{(\Delta x_1)^p - (\Delta x_0)^p}{(\Delta x_1)^p - (\Delta x_0)^p}, \tag{6.2}$$

we can estimate the convergence order p of the solution, however, in insufficient resolution simulations higher order terms matters. In our case, a convergence to sixth order is expected because of the numerical scheme used. Because the resolution Δx_i is related to the number of points N_i at that resolution as $\Delta x_i \sim 1/N_i$, we compute the sixth order convergence factor to be:

$$\frac{(\frac{1}{N_1})^6 - (\frac{1}{N_0})^6}{(\frac{1}{N_2})^6 - (\frac{1}{N_1})^6} = \frac{1 - (\frac{N_1}{N_0})^6}{(\frac{N_1}{N_2})^6 - 1} \approx 4.23. \tag{6.3}$$

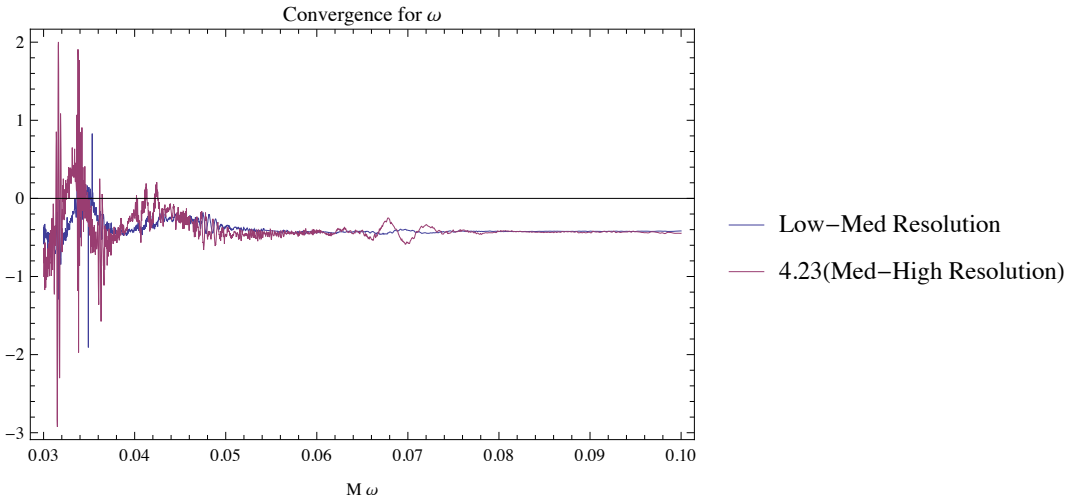

Figure 6.5: Convergence test over the orbital frequency shows the solution to converge at sixth order.

To perform the convergence test for the orbital frequency, and to be sure that we are comparing over the same points, we need to align the three solutions. But instead of working with $w_{orb}(t)$ we found it suitable to work with $t(w_{orb})$ so we can align it at

the desired value of w_{orb}. The estimation of the convergence order is consistent with the numerical scheme used, which is sixth order.

However, as stated in Sec. 5.4, the convergence test is not as simple as before here. Figure 6.6 does not show the expected convergence order, just shows third order convergence. The separation is indeed a more gauge-dependent quantity than the orbital frequency, which may be the reason for its poorer convergence.

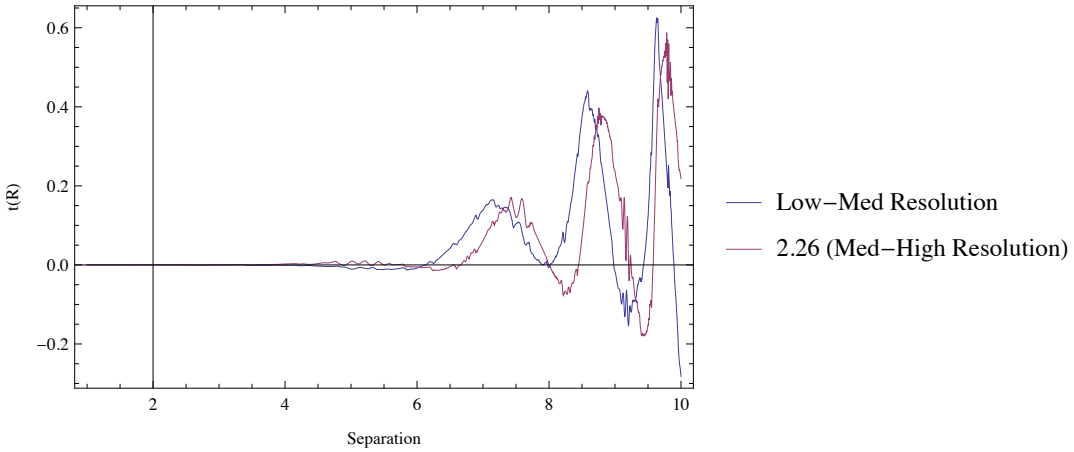

Figure 6.6: Convergence test over the orbital separation, not a clear convergence is shown.

6.1.2 Richardson Extrapolation

Apart from testing the accuracy and the reliability of our solution. We can check the error ϵ we made by using the Richardson Extrapolation [50]. Writing the obtained solution as (6.1), using two resolutions we can solve the system of equations for R_{exact}, and then compare with the higher resolution solution.

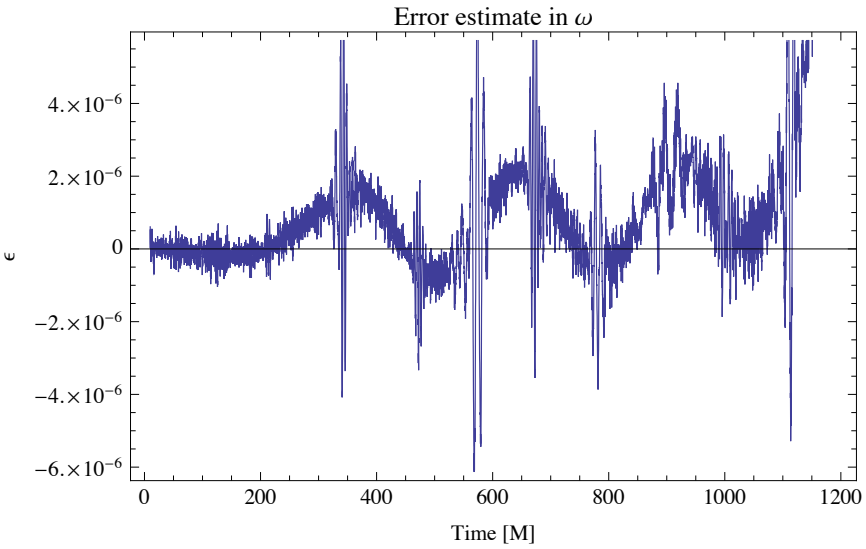

Figure 6.7: Error estimation from the Richardson extrapolation for the orbital frequency.

Figure 6.7 shows an estimate for the error made in the orbital frequency in the higher resolution solution. We can see that the error is $\mathcal{O}(10^{-6})$ before the merger. That indicates that our runs are well resolved.

6.2 Precession

In our case, because of the general spin configuration, where the spins are not in the direction of the orbital angular momentum, precession occurs in the spin vectors and the orbital plane, which in this case is not conserved.

In the equations of motion of the effective one-body approach (3.16-3.19), the spin-orbit term (3.6) is the leading term for the precession during the inspiral. When the effects of radiation-reaction are included, it is usual that the total angular momentum $\mathbf{J}$ remains fixed and the orbital angular momentum $\mathbf{L}$ precess over that direction. However, in a configuration where $\mathbf{L}$ and $\mathbf{S}$ are anti-parallel and the mass-ratio is large, at large separations when $r \to \infty$ then $\mathbf{L} \to \infty$; but when the separation is small, $\mathbf{L}$ decreases due to radiation reaction and $|\mathbf{S}|$ will eventually be higher than $|\mathbf{L}|$, then $|\mathbf{L}+\mathbf{S}|$ will go through zero and make the orbital plane tumbles in space [51].

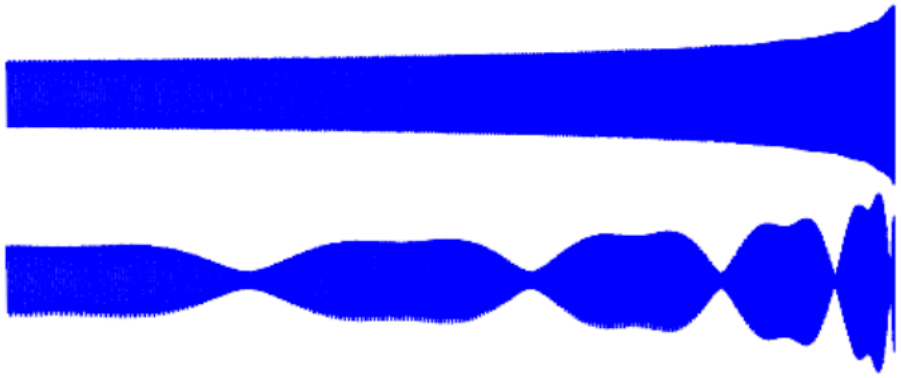

Figure 6.8: Gravitational wave waveform seen if the observer is oriented along the $\mathbf{J}$ *direction (upper figure), and if the observer is oriented perpendicular to* $\mathbf{J}$ *(lower figure). Source: [52]*

The binary emits the gravitational wave signal predominantly in the direction perpendicular to its orbit. So, for a non-precessing binary, this direction would be fixed and the waveform won't vary with the binary orientation. However, in precessing binaries, waveform will strongly depend on the observer orientation [52] as seen in Figure 6.8.

To avoid the modulation in the waveform due to precessing effects, the numerical code tracks the precession of the orbital frame. It identifies the direction of the dominant emission and sits in the frame where the z-direction of the numerical frame is aligned with the orbital angular momentum $\mathbf{L}$ [53].

6.3 Results

Gathering together all the points that the punctures have visited we find the orbits of both black holes before they merge. Figure 6.9 shows the last around 5 orbits of the inspiral phase and the behaviour of the black holes after the ISCO.

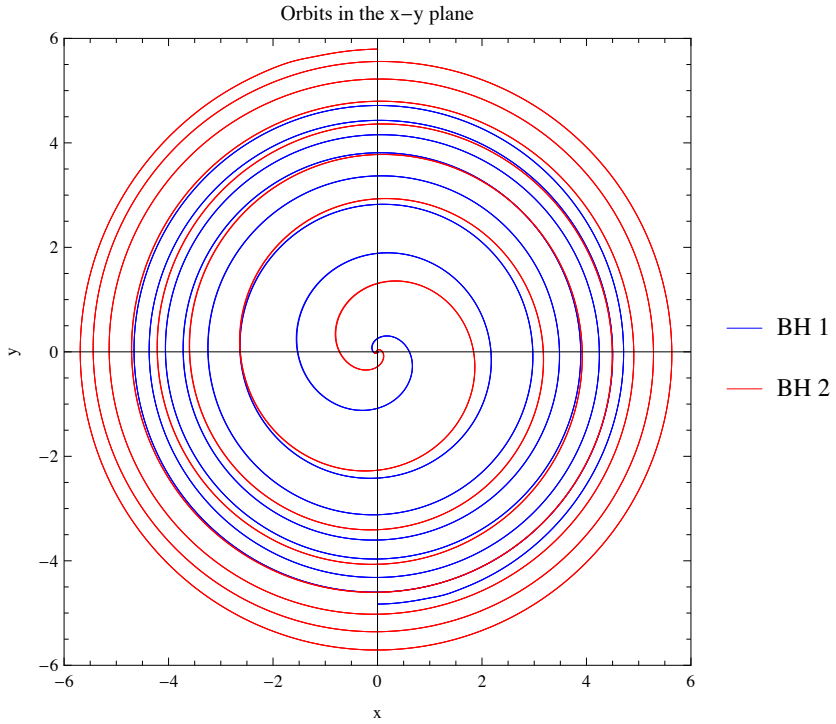

Figure 6.9: Orbits described by the black holes projected on the x-y plane.

Both black holes approximate describing closer orbits as they lose energy via the emission of gravitational waves. The heavier black hole (blue curve) moves in a tighter orbit. As the mass ratio q grows, the orbit of the heavier black hole would be tighter, in contrast with the equal-mass binary, where both orbits would look the same. Also the number of stable orbits depends on the mass ratio, the higher the mass ratio is, the fewer stable orbits before the ISCO.

However, because the binary is precessing, the orbits are drawn in a 3-dimensional space. We can see the precession of the orbital plane in Figure 6.10. In addition, we see that when the binary has merged, during the ringdown stage, the remaining black hole is still moving. This is known as the recoil velocity, that can take values of around 5000km/s in a equal-mass black hole binary with the same spin magnitude and the spin direction optimally oriented, see Sec. 6.3.2.

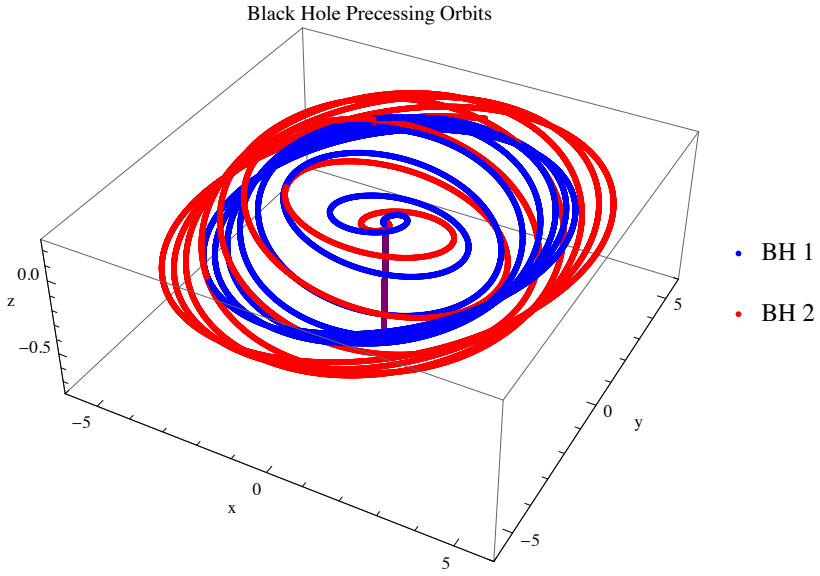

Figure 6.10: Orbits followed by the black holes in full 3D. Once the black holes ahve merged, the remnant black hole moves away from the orbital plane with a recoil velocity of $v = 402.12 km/s$.

6.3.1 Final Mass and final spin

The final mass that the remaining black hole should have can be computed from the lost energy due to gravitational wave radiation. So, taking into account the ADM mass from where the numerical relativity simulation is started and the energy radiated in the process, we can estimate the mass of the black hole resulting from the merger. The energy contained in the final space-time would be $M_f = M_{ADM} - E_{rad}$ (5.7).

Figure 6.11a shows the energy radiated at each time step. The maximum of the curve is where the two initial black holes merge giving way to the final black hole. During the merger, most of the energy is radiated. The integral of this curve will lead to energy radiated as a function of time (Figure 6.11b), after the merger, where no more energy is radiated, the energy tends to the energy radiated during the numerical simulation.

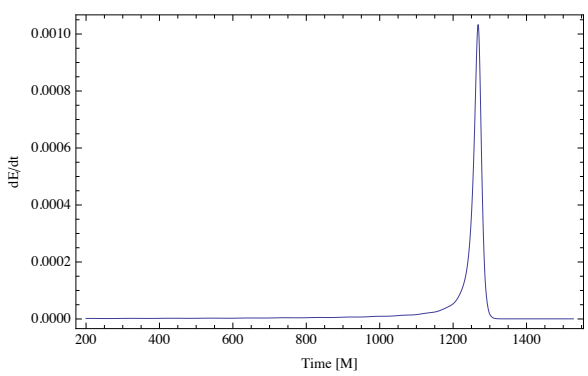

(a) Energy radiated at each time step.

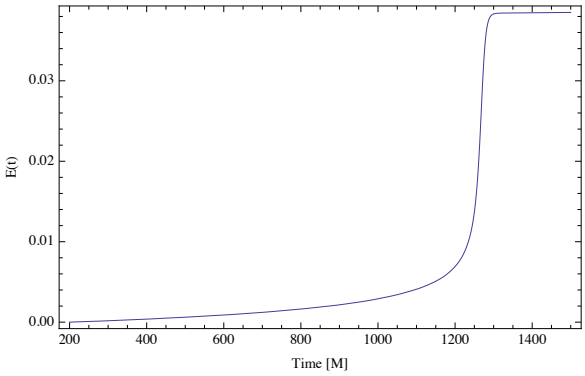

(b) Energy radiated as a function of time.

After the merger, we have a value of $E_{rad} \approx 0.0385$; and, providing that initially the $M_{ADM} \approx 0.9903$, we find a mass for black hole resulting of the merger of $M_f \approx 0.9518$. Around 3.9% of the initial energy has been radiated away in the form of gravitational waves.

In order to compute the final spin of the remaining black hole, the same procedure is done but with the angular momentum **J** instead of the energy. In the ringdown stage, when a Kerr black hole is formed from the merger, the angular momentum is computed to be $|\mathbf{J}| \approx 0.62$ mostly in the z-direction ($\{J_x, J_y, J_z\} = \{1.3 \times 10^{-3}, -5.1 \times 10^{-3}, 0.62\}$). So, the Kerr parameter of the final black hole is estimated to be $a \approx 0.69$.

6.3.2 Final Recoil Velocity

As suggested by the orbits, a final recoil velocity appears after the merger. This is an effect of the loss of lineal momentum radiated away via gravitational waves. Therefore, the final velocity can be computed using the lineal momentum reached in the ringdown phase and the mass of the remaining black hole.

In this case, where a general spin configuration is used, the lineal momentum in the three directions $\{x, y, z\}$ have to be considered (Figure 6.12). Given the mass of the remnant black hole, the final recoil velocity can be computed using the total lineal momentum, this is estimated to be $v = 402.13$km/s. As we see, mostly the lineal momentum is radiated in the z-direction, so the final velocity would be pretty aligned with the z-axis, consistent with the motion we see from Figure 6.10.

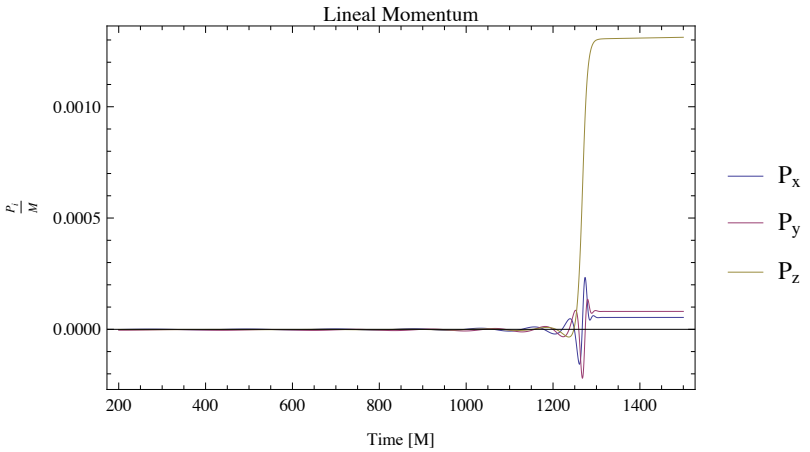

Figure 6.12: Lineal momentum as a function of time for the three $\{x, y, z\}$ directions.

Typical final velocities for stellar mass binary black hole configurations are around 100km/s for non-spinning configurations, and around 400km/s for spinning binaries, depending on the spin configuration for both black holes [54, 55, 56]. An understanding of this final black hole velocity give some insights about the formation and populations of black holes [57].

Typical galaxy escape velocities are around 500km/s, so accurately determining the final recoil velocity of a binary black hole merger will help in the determination of the formation of new binary configurations. With the detection of GW150914, where the existence of black holes and binaries were confirmed, and future gravitational wave observations, a better understanding of the recoil velocity distribution will be gained.

6.4 Waveform

Via binaries such as Cygnus X-1 we can deduce that black holes and binaries exists, moreover, there is a strong evidence that a supermassive black hole is located at the center of our galaxy, the Milky Way. However, the only way to direct detect black holes in a binary is via the emission of gravitational waves, *e.g.*, the gravitational waveform generated by its coalescence. There are catalogues of gravitational wave waveforms to be directly compared with the data recorded by the actual detectors. In this section the waveform from this binary configuration will be computed from the simulation information. As discussed in Chapter 7, one can extract information of this waveform comparing the result to the

detected data via match filtering techniques.

6.4.1 Ψ_4

As stated, the usual approach to extract gravitational waves from black hole simulations is the Newman-Penrose formalism. In this formalism, the Ψ_4 is computed, split into different harmonic spherical contributions. Figure 6.13 shows the dominant $l = 2$, $m = 2$ mode gravitational wave signal. The blue curve shows the real part of the Ψ_4 and the red curve shows the absolute value of Ψ_4, which shape is similar to Figure 6.11a. As expected, it has the maximum around the merger.

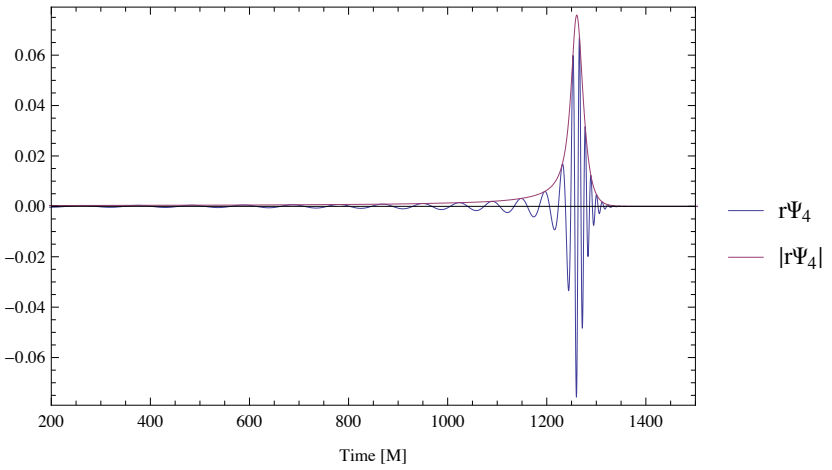

Figure 6.13: Real part and absolute value of Ψ_4 for the $l = 2$, $m = 2$ mode.

The amount of energy carried by gravitational waves can only be non-ambigous defined at infinity. Because gravitational waves are generated by massive accelerated objects, the equivalence principle does not allow us to fix a preferred reference frame where we could see gravitational waves at a finite distance. Thus, the extraction has to be done by an inertial observer at infinity. However, in a numerical simulation we have a finite numerical domain. So, the extraction has to be done at a sufficiently large radius but with sufficient resolution so we have an accurate solution. In this case, the extraction was done at $R = 65M$ which is located at $l = 7$ numerical refinement level, the largest radius with the highest resolution. The choice of $R = 65M$ is because it is the most resolved radius, going further implies more computational expensive simulations, because outer levels would have to be better resolved. The election of this radius turn out to be sufficient, see Sec. 7.4.

6.4.2 Fixed Frequency Integration (FFI) Method

In order to obtain the strain h from the Ψ_4 two integrations in the time domain are needed:

$$h = h_+ - ih_x = \int_{-\infty}^{t} dt' \int_{\infty}^{t'} dt'' \Psi_4, \tag{6.4}$$

where in practice the integration is performed from the beginning of the simulation, not from $t = -\infty$. The direct integration of (6.4) in the time domain, will produce problematic artifacts.

However, we can transform the problem to the frequency domain where the integrated function $f(t)$ now takes the form:

$$\tilde{f}(\omega) = \mathcal{F}[f] = \int_{-\infty}^{\infty} \mathrm{e}^{-i\omega t} f(t) dt, \tag{6.5}$$

and so, the Fourier transform of the integral,

$$\mathcal{F}\left[\int_{-\infty}^{t} dt' f(t')\right] = -i\frac{\tilde{f}(\omega)}{\omega}, \tag{6.6}$$

thus, in the frequency domain, we can perform a time integral by just dividing by ω. In (6.6), we see why the integration in the time domain is not a good choice; when we go to lower frequencies, we find an indetermination.

Now, the strain in the frequency domain will depend on Ψ_4 like:

$$\tilde{h}(\omega) = -\frac{\tilde{\Psi}_4(\omega)}{\omega^2}. \tag{6.7}$$

The problem of the lower frequencies is solved by the FFI method [58] that consists, then, in evaluating (6.7) using the prescription:

$$\tilde{F}(\omega) = \begin{cases} -i\tilde{f}(\omega)/\omega_0, & \text{if} \quad \omega \leq \omega_0, \\ -i\tilde{f}(\omega)/\omega, & \text{if} \quad \omega > \omega_0., \end{cases} \tag{6.8}$$

where the parameter ω_0 is the lowest expected physical frequency for a given mode. So, we can get the strain in the frequency domain by just performing $(-i\tilde{\Psi}_4(\omega)/\omega_0)^2$ or $(-i\tilde{\Psi}_4(\omega)/\omega)^2$ when corresponds. Then, to get the strain $h(t)$ in the time domain, we just need to transform back from the Fourier domain.

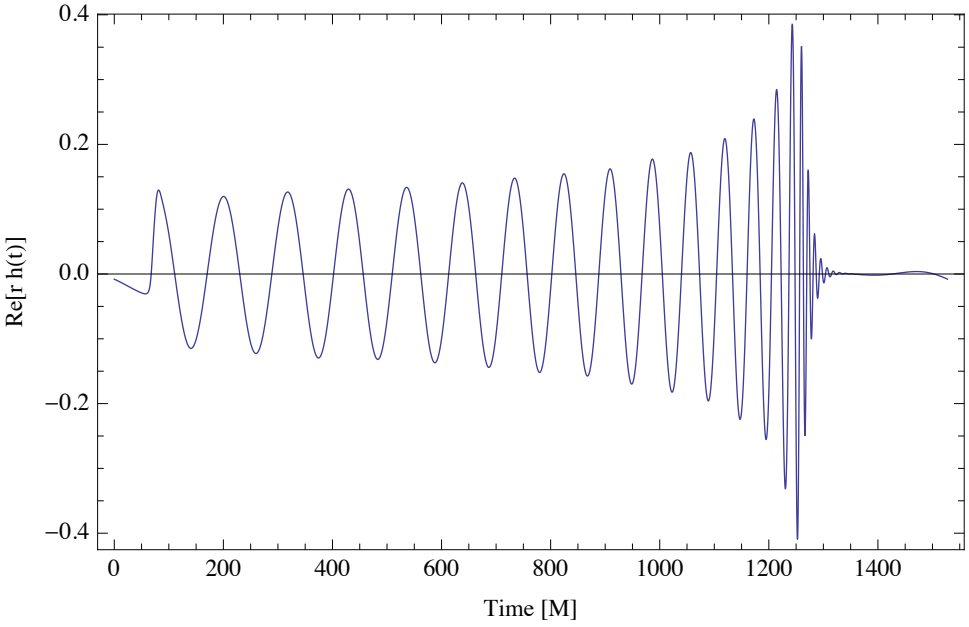

Figure 6.14: Waveform from the dominant $l = 2$, $m = 2$ mode; computed with the FFI method.

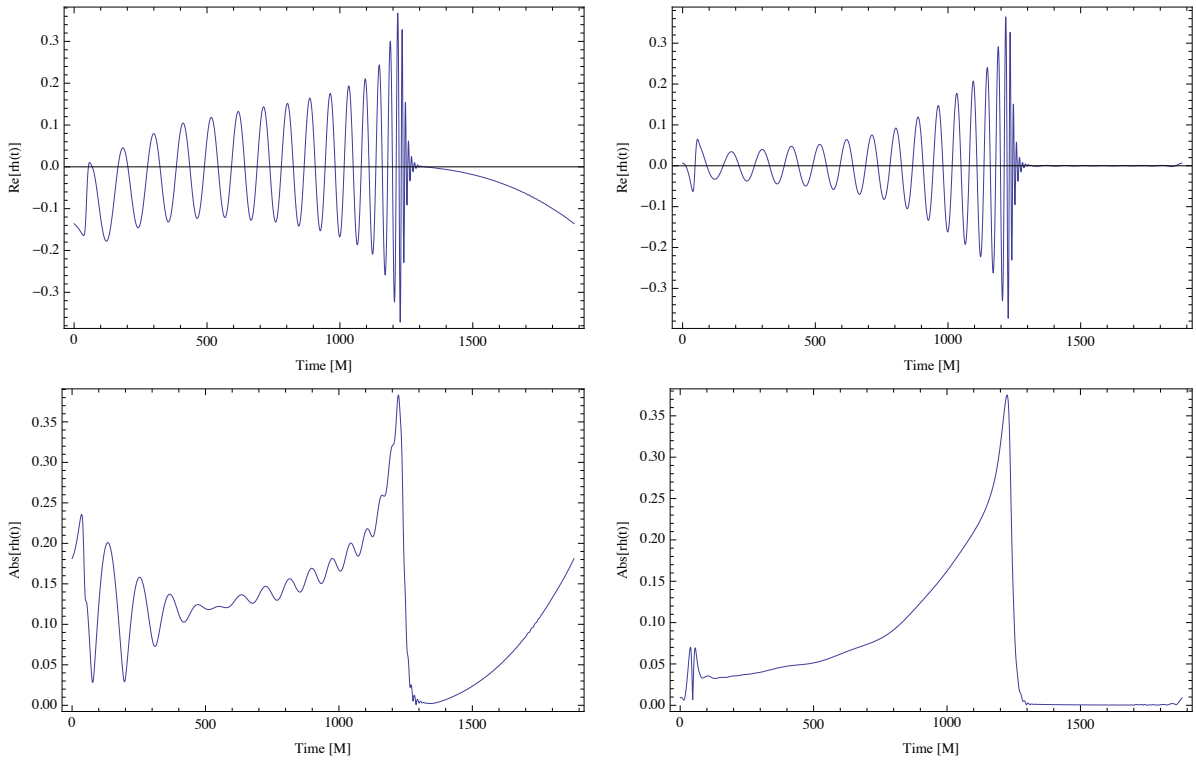

Figure 6.15: Waveforms coming from a bad election of the parameter ω_0. Left: ω_0 is underestimated, $\omega_0' = 0.1\omega_0$. Right: ω_0 is overestimated, $\omega_0' = 2\omega_0$.

The correct setting of the parameter ω_0 allow us to get a representation of the waveform in the time domain which is free of low frequency drifts. Using this method, we obtained $\omega_0 = 7.2 \times 10^{-3}$, and the waveform obtained is shown in Figure 6.14. If the parameter ω_0 is not correctly set, we may miss information or get extra artifacts in the waveform, as we see in Figure 6.15.

Chapter 7

The Detected Gravitational Wave Signal

The gravitational waves created in a source such as the coalescence of two black holes perturb the surrounding metric and move away from the binary at the speed of light. As stated, gravitational waves travels large distances keeping the information of the source unaffected due to their weak interaction with matter. The gravitational wave-front will eventually reach the Earth, provided with accurate detectors to measure them. The actual ground-based detectors such as LIGO, VIRGO or GEO600; and the future space-based gravitational wave detector LISA [59], use interferometric techniques to measures the change in the relative length difference of the two arms.

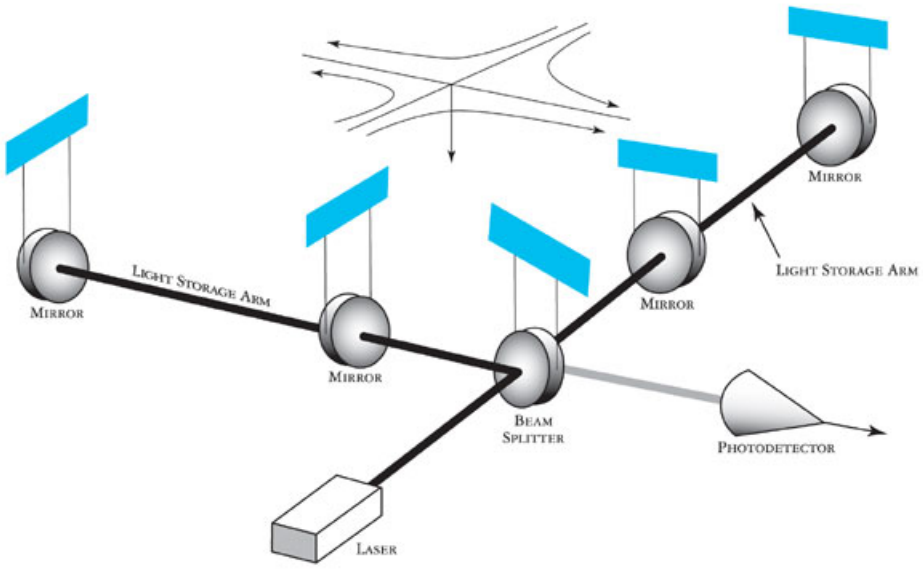

Figure 7.1: Simplified diagram of an interferometric detector. Source: www.ligo.org

In order to be able to identify the waveform (Figure 6.14), computed using Numerical Relativity techniques, in the data recorded by the detector; a set of transformations are needed to convert the waveform in the source frame to the measured relative length changes of the detector arms in its frame.

7.1 Spin Weighted Spherical Harmonics

In first place, we have to express the radiation computed on its basis. The computation of the Newman-Penrose scalar Ψ_4 gives us the gravitational radiation in terms of the spherical harmonics Y^s_{lm} of spin weight -2. For our purposes, to compare the computed waveform to the recorded real data, it's enough to consider the dominant $l = |m| = 2$ modes. So, a first step, would be to express the gravitational radiation weighted by its corresponding spherical harmonic. The $l = 2$, $m = \pm 2$ spin -2 spherical harmonics are:

$$Y^{-2}_{22} = \frac{1}{2} e^{i2\phi_0} \sqrt{\frac{5}{\pi}} \cos^4\left(\frac{\theta_0}{2}\right), \tag{7.1}$$

$$Y^{-2}_{2-2} = \frac{1}{2} e^{-i2\phi_0} \sqrt{\frac{5}{\pi}} \sin^4\left(\frac{\theta_0}{2}\right), \tag{7.2}$$

where the ϕ_0 and θ_0 are consistent with the GW150914 event [10], and turn out to be $\phi_0 = 0°$ and $\theta_0 = 150°$.

7.2 Gravitational Wave Signal in the Detector Frame

The gravitational waveform computed in previous chapters, is the waveform that emerges from the specific configuration of a binary black hole coalescence. However, from the detector point of view, located in the Earth in our case; and with the source at a huge distance away in a particular region of the universe, a set of rotations [60] has to be applied to express the gravitational wave signal in the detector frame.

Let's first describe the coordinate systems involved:

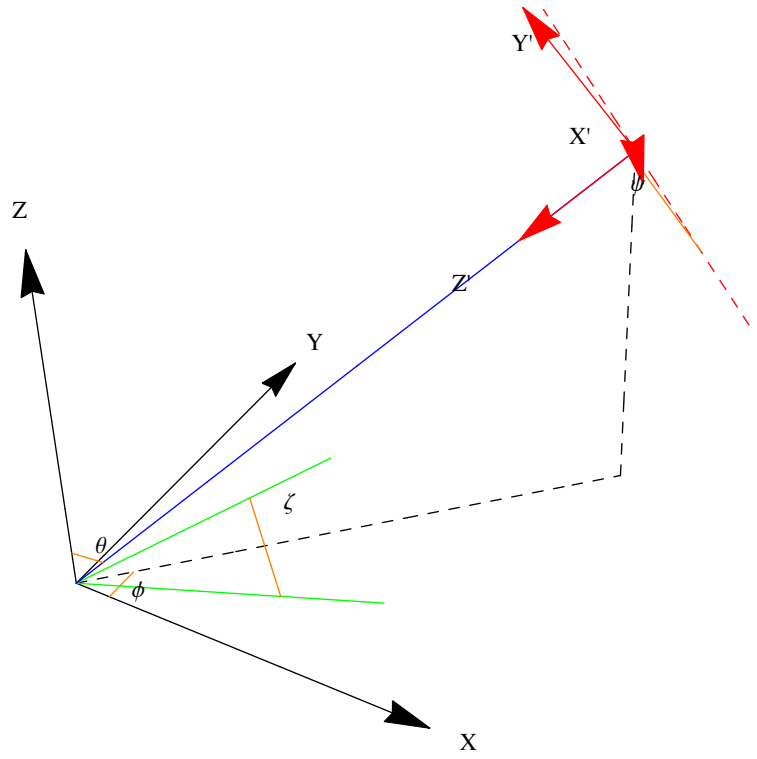

Figure 7.2: Reference frames attached to the detector (black) and to the wave-front (red).

A first reference frame attached to the detector (black), with the detector arms contained in the $X-Y$ plane and the Z direction pointing to the zenith. In Figure 7.2, a sketch of the frames is represented; in general, the detector arms (green) would form an angle of $\zeta°$, but in our case, the LIGO detectors, it is $\zeta = 90°$. The second reference frame is the one attached to the travelling wave (red), where the gravitational wave travels along the Z' direction.

In order to transform the wave reference frame in the detector's frame, a set of three rotations is needed: (i) rotate the wave plane $-\phi°$ around the Z axis, so the planes $X'-Y'$ and $X-Z$ match; (ii) rotate the same plane $(\pi-\theta)°$ around the Y axis to let both Z and Z' axis match; and finally (iii) rotate again the wave plane $\psi°$ around the Z axis, so the $\{X', Y'\}$ axis and $\{X, Y\}$ coincide. With these rotations, we can see how the amplitude

of the gravitational wave is measured in the detector frame. So, the rotation matrix M would be:

$$M = \begin{pmatrix} \cos\phi & \sin\phi & 0 \\ -\sin\phi & \cos\phi & 0 \\ 0 & 0 & 1 \end{pmatrix} \cdot \begin{pmatrix} -\cos\theta & 0 & \sin\theta \\ 0 & 1 & 0 \\ -\sin\theta & 0 & -\cos\theta \end{pmatrix} \cdot \begin{pmatrix} \cos\psi & -\sin\psi & 0 \\ \sin\psi & \cos\psi & 0 \\ 0 & 0 & 1 \end{pmatrix} \tag{7.3}$$

$$= \begin{pmatrix} -\cos\theta\cos\phi\cos\psi + \sin\phi\sin\psi & \cos\psi\sin\phi + \cos\theta\cos\phi\sin\psi & \cos\phi\sin\theta \\ \cos\theta\cos\psi\sin\phi + \cos\phi\sin\psi & \cos\phi\cos\psi - \cos\theta\sin\phi\sin\psi & -\sin\theta\sin\phi \\ -\cos\psi\sin\theta & \sin\theta\sin\psi & -\cos\theta \end{pmatrix}, \tag{7.4}$$

and the measured gravitational wave amplitude, h', in terms of the emitted signal h, is $h' = M \cdot h \cdot M^T$, where M^T is the transposed M matrix, and

$$h = \begin{pmatrix} h_+ & h_x & 0 \\ h_x & -h_+ & 0 \\ 0 & 0 & 0 \end{pmatrix}. \tag{7.5}$$

So, we find the so called antenna beam patterns, for each polarization:

$$F_+ = \frac{1}{2}(1 + \cos^2\theta)\cos 2\phi\cos 2\psi - \cos\theta\sin 2\phi\sin 2\psi, \tag{7.6}$$

$$F_x = -\frac{1}{2}(1 + \cos^2\theta)\cos 2\phi\sin 2\psi - \cos\theta\sin 2\phi\cos 2\psi, \tag{7.7}$$

that depend on the sky location $\{\theta, \phi\}$ and on the polarization angle ψ. The $\{+, x\}$ subscript denote the different polarizations; so, the measures signal would be

$$h = F_+ h_+ + F_x h_x. \tag{7.8}$$

7.2.1 Sky Location

A single ground-based detector is an all-sky monitor for the signal. A network of these detectors is needed in order to well determine the location in the sky. Actually, only two LIGO detectors are available: Hanford [61] and Livingston [62]. With only two detectors and thanks to the time delay that the signal takes to arrive from one detector to the other, we can locate the position of the source within a ring in the sky. Given that the time delay of GW150914 between the two observatories was 6.9ms, a region of 150deg^2 (50% probability) and a region of 610deg^2 (90% probability) is defined in Figure 7.3.

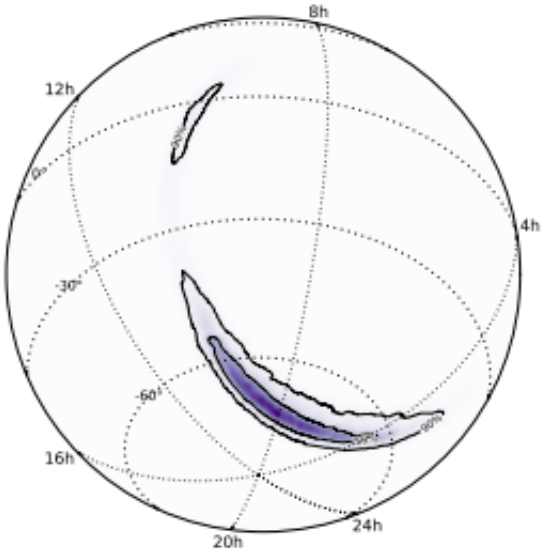

Figure 7.3: Sky location of GW150914 given in terms of right ascension α (measured in hours) and declination δ (measured in degrees). Source: [10].

Now, we can use the most probable sky location to construct the detector measured gravitational wave signal using equation (7.8). But, for that, we need to convert the location in terms of right ascension and declination to the variables used to define the antenna beam patterns, which are azimuth (ϕ) and altitude (θ), at the time the signal arrived.

In order to compute the sky location in terms of azimuth and altitude, we need to know the latitude (LAT) and longitude (LON) of the detector (Livingston's detector since the signal hits there first), the Right ascension and declination of the source (given by Figure 7.3), and the time that happened, that in our case is September 14, 2015 at 09:50:45 UTC. So, azimuth and altitude are given by [63]:

$$\sin\theta = \sin\delta \sin LAT + \cos\delta \cos LAT \cos HA, \tag{7.9}$$

$$\cos\phi = \frac{\sin\delta - \sin ALT \sin LAT}{\cos ALT \sin LAT}, \tag{7.10}$$

where HA stands for Hour Angle, that can be calculated as $HA = LST + \alpha$; where LST is the local sidereal time, calculated with the time of the event.

So, putting all together, the computed values for the azimuth and altitude are

$$\theta = 47^\circ \quad 3' \quad 8'', \tag{7.11}$$

$$\phi = 4^\circ \quad 10' \quad 11'', \tag{7.12}$$

which are consistent with the 6.9ms of delay, given the separation of the two detectors.

7.2.2 The Detected Wave

In the previous chapter, in Figure 6.14, we find a plot of the waveform as it is computed in the Numerical Relativity simulation. However, to identify the pattern of the waveform produced into the real data, we need to scale the waveform from the simulation with the distance and recover the physical units. From the simulation we computed $rh(t)$, which is finite for $r \to \infty$. But we want to compute $h(t)$, that is a metric, so

$$h(t) \sim \frac{1}{r}(rh(t)), \tag{7.13}$$

now, we have to recover the source distance from [10], which is $r = 410$Mpc.

Recovering physical units, expressing the Ψ_4 in its spin weighted spherical harmonic basis and performing the whole set of transformations described above, we find the strain of the gravitational wave as we would see it in the detector (in the absence of noise):

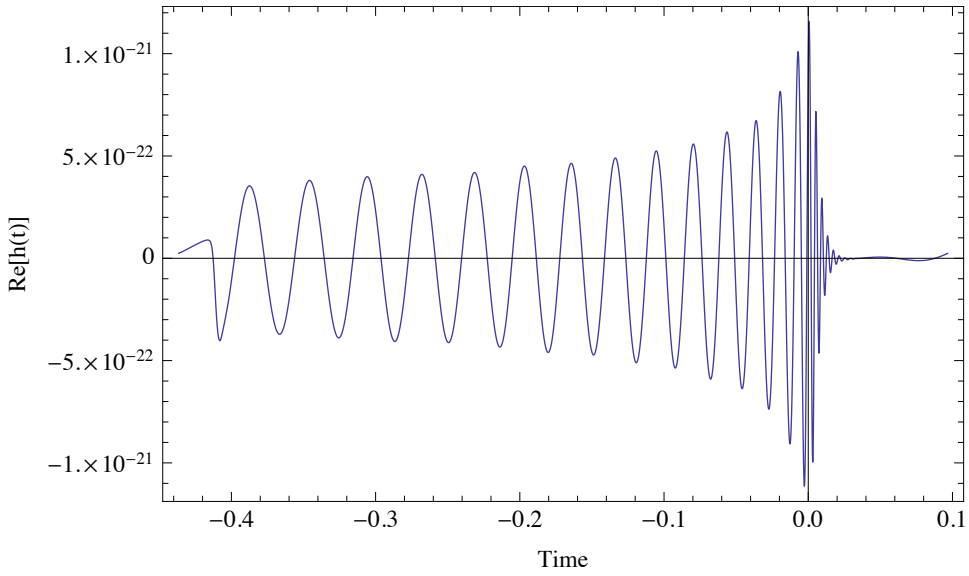

Figure 7.4: Dominant $l = m = 2$ mode of the signal as seen in the detector.

Where we see that we recover the typical amplitude order of 10^{-21} in physical units.

7.3 GW150914 Data Analysis

The signal described above, in Figure 7.4, would be the signal we would find in a detector with no noise. However, actual detectors have many noise sources that we have to take into account. So, we can express the data recorded by the detector as

$$s(t) = n(t) + h(t), \tag{7.14}$$

where $s(t)$ is a time series directly recorded by the detector; $h(t)$ is the eventual signal given by (7.8); and $n(t)$ is the noise assumed to be Gaussian, stationary and with zero mean, defined by its one-sided power spectral density (PSD) $S_n(f)$ [64]

$$|\tilde{n}(f)\tilde{n}^*(f')| = \frac{1}{2}\delta(f - f')S_n(f), \tag{7.15}$$

here, $\tilde{n}(f)$ denotes the Fourier transform according to, for a time series $x(t)$,

$$\tilde{x}(t) = \int_{-\infty}^{\infty} \mathrm{e}^{i2\pi ft} x(t)\, dt. \tag{7.16}$$

The amplitude spectral density ASD, square root of the PSD of the LIGO detectors, by the day of the event, is shown in Figure 7.5.

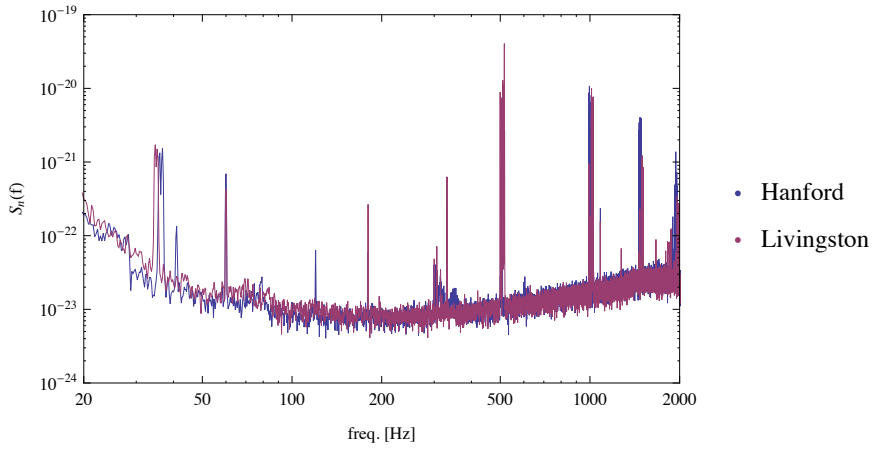

Figure 7.5: Amplitude spectral densities for Hanford (blue) and Livingston (red) observatories. Source: Own Production, from data released by LIGO in the Open Science Center [65].

Now, using the definition of the Fourier transform, and the PSD of the noise; together with the definition of the Wienner scalar product between two time series $a(t)$ and $b(t)$,

$$(a|b) \equiv \int_{-\infty}^{\infty} \frac{\tilde{a}^*(f)\tilde{b}(f) + \tilde{a}(f)\tilde{b}^*(f)}{S_n(f)}\, df = 4\mathrm{Re}\int_0^{\infty} \frac{\tilde{a}^*(f)\tilde{b}(f)}{S_n(f)}, \tag{7.17}$$

we are ready to compute one feature of the gravitational wave signal with respect to the detector, its signal-to-noise ratio (SNR): the ration between the filtered signal and the root-mean-squared of the filtered noise,

$$\mathrm{SNR}^2 = (h|h) = 4\int_0^\infty \frac{|\tilde{h}(f)|^2}{S_n(f)}\,df. \tag{7.18}$$

The SNR is a significant quantity if we want to talk about a detection: in order to confirm that a detection has been made, the SNR has to be grater than 8. In our case, with our template of the GW150914 event, and with the $S_n(f)$ of the day of the event, the SNR computed is around 29; compatible with [9], where an SNR of 24 is found.

In the previous chapter, we evaluate the differences between the different simulations performed, of resolutions R_0, R_1 and R_2. But now, it's useful to evaluate these differences between the waveforms computed in each simulation, but in the detector point of view. The first step, would be to compute the time and phase shift such that the miss-match between two waveforms is minimum, where the miss-match is defined by

$$1 - \mathcal{M} = 1 - \max_{t_c,\phi_c}\left[\frac{\langle\tilde{h}_1|\tilde{h}_2\rangle}{\sqrt{\langle\tilde{h}_1|\tilde{h}_1\rangle}\sqrt{\langle\tilde{h}_2|\tilde{h}_2\rangle}}\right], \tag{7.19}$$

the computed miss-match between the waveforms coming out from the different resolution simulations is of the order $\mathcal{M} \sim 10^{-5}$. The miss-match computed between the highest resolution waveform and the waveform from the SXS database [66], is of the order $\mathcal{M} \sim 10^{-3}$.

Once we have the waveforms aligned in the time domain, to see whether the detector sees any difference between the waveforms, we need to calculate the differences between them in the time domain, $\delta h(t) = h_1(t) - h_2(t)$, and transform to the frequency domain to compute $\langle\delta\tilde{h}|\delta\tilde{h}\rangle$. If that inner product satisfies the criteria

$$\langle\delta\tilde{h}|\delta\tilde{h}\rangle < 1, \tag{7.20}$$

we can say that the two waveforms are indistinguishable [67, 68]. In our case, it could be also an accuracy check, and we find:

	h_0	h_1	h_2
h_0	0	1.50	1.52
h_1	1.50	0	0.26
h_2	1.52	0.26	0

Table 7.1: Results of (7.20) for waveforms h_i, obtained from the three different resolution simulations (R_0, R_1 and R_2).

From Table 7.1, we can see that the lower resolution simulation (R_0) is not well resolved, the detector could distinguish its waveform from the other two simulations. This is only a problem of resolution, because for the other two simulations (R_1 and R_2), with a larger number of points, we see that the detector couldn't distinguish its waveforms. Moreover, we can do the same analysis between the most resolved simulation (R_2) waveform, and the waveform form the SXS database [66] used to match the real data in [9]. Now, the waveforms are different not just in the resolution of the simulation, but in the configuration of the binary black hole: we compare a precessing binary black hole with a non-precessing one. The parameter estimation for GW150914, allows both precessing and non-precessing sources. Computing (7.20) for these two waveforms, we see that,

$$\langle \delta\tilde{h} | \delta\tilde{h} \rangle = 0.79 < 1, \tag{7.21}$$

satisfies the criteria; the actual LIGO observatories could not distinguish between these two different configurations.

7.4 Comparison to Real Data

At this point, when an accurate waveform is computed in the detector frame, we can start looking for this pattern in the real data recorded by the detectors to eventually find a gravitational wave signal.

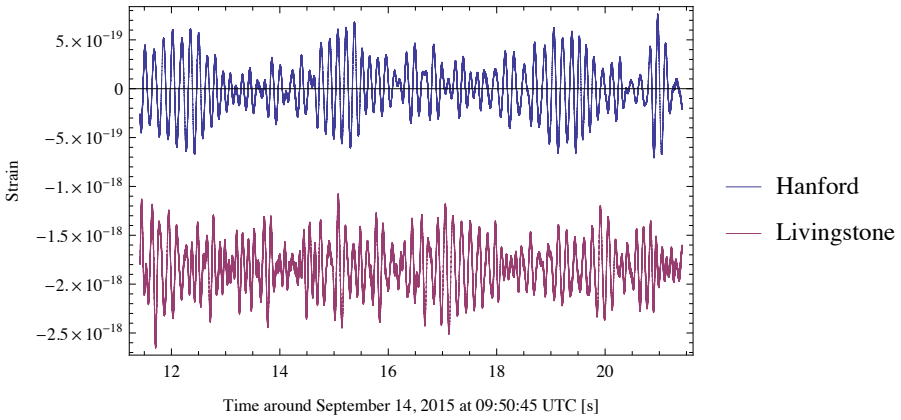

Figure 7.6: Actual data near GW150914. Source: Own production from data released by LIGO.

In Figure 7.6 we can see the real data recorded by the LIGO observatories near the time of the September 14 event. One can eventually find a gravitational wave signal buried in the noise, with some signal processing. To have an idea of the frequency content of the data, we can see in Figure 7.5 that below 20Hz, the recorded data won't contribute to the SNR because the noise is so high in that region. The sample rate of LIGO is fs= 16kHz, so nothing above the Nyquist frequency (fs/2) of 8kHz can be captured. However, to handle with lighter files, the data has been downsampled to fs= 4096Hz. Also from Figure 7.5, we can see that the data is colored, *i.e.* noise fluctuations are higher at low and high frequency; so a first step to better see the weaker signals is to "whiten" the data by dividing it by the noise amplitude spectrum in the Fourier domain. In addition, to get rid of the high frequency noise, the data will be also band-passed.

Doing the above described procedure to both the data and the Numerical Relativity template computed in previous sections; we are ready to find the gravitational wave signal, described by the waveform (Figure 7.4), buried in the noisy data. The optimal way to find a known signal in this kind of data is via matched filtering searches. LIGO uses an elaborate software suite to find the patterns that describe the waveforms computed via Numerical Relativity in the data recorded by the detectors. Facing a new gravitational wave signal candidate in the data requires a computationally-intensive search over all the waveform templates (about 250 000) computed from different binary configurations. However, here only one waveform template (Figure 7.4) is used to match in the data. An outline of this matched filtering technique can be found in [69, 70].

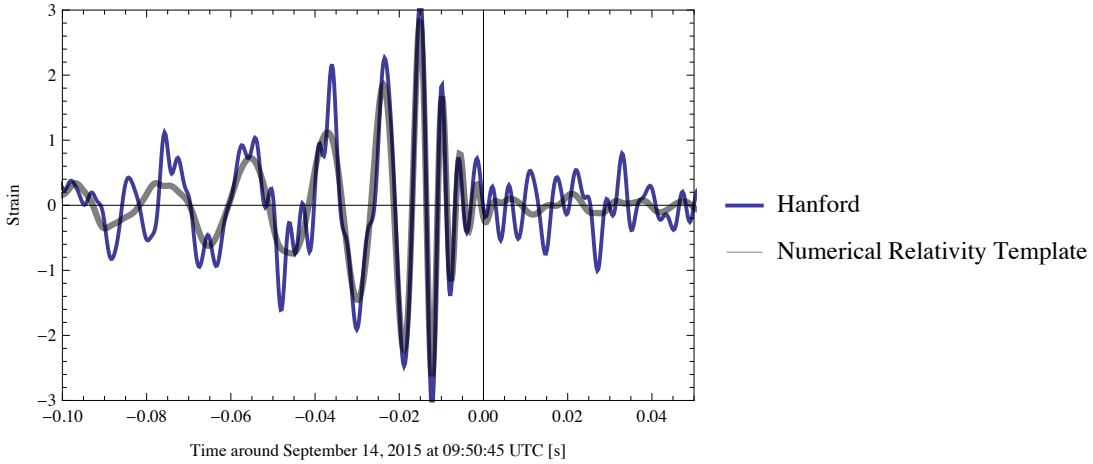

Figure 7.7: Numerical Relativity template matched in the data from the Hanford observatory.

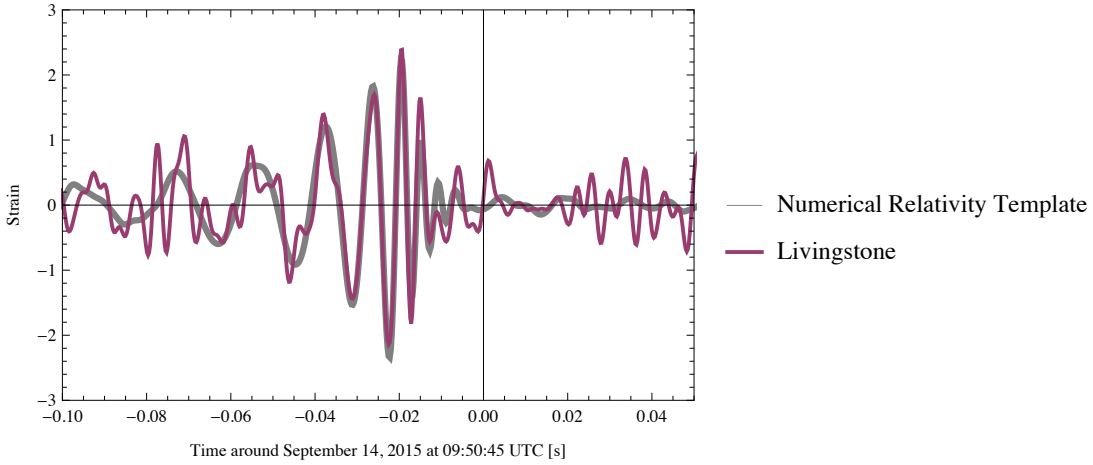

Figure 7.8: Numerical Relativity template matched in the data from the Livingstone observatory.

We can see, in both Figure 7.7 and Figure 7.8, that the waveform template computed via Numerical Relativity is easy recognizable in the observed data.

Chapter 8

Conclusions

During this thesis, an accurate precessing waveform model has been constructed via analytic and Numerical Relativity techniques, to finally compare the resulting template with the real data recorded by the LIGO observatories to conclude that a first event of a gravitational wave signal was detected. The source of the signal was a black hole binary, formed by two black holes of individual masses $36M_{\odot}$ and $29M_{\odot}$ respectively located at a luminosity distance of 410Mpc corresponding to a red-shift $z = 0.09$.

The effective one-body approach is a non-perturbative re-summation of the standard Post-Newtonian expanded results. Its analytical results define good initial conditions for the Numerical Relativity simulations near the ISCO, and lead to more robust evolution to these simulations. The main advantage of this analytical model is to save computational time by starting the NR simulation not from a beginning stage of the inspiral phase but from a stage where only a few orbits are left for the merger, where big computational resources are needed in order to well resolve that phase.

The mathematical description of the problem, to solve the Einstein field equations in vacuum, turn out to be a key ingredient for the Numerical Relativity breakthroughs in 2005. The BSSN equations, nowadays used in most numerical codes, came from writing the Einstein field equations as an well-posed initial value problem with suitable stability conditions for long-term simulations. The continuous development of numerical codes to produce accurate simulations efficiently is also important.

Nonetheless, even if the simulation is accurate enough, without the contribution of some signal processing, the comparison between the data from the detector with the waveform template won't lead to successful results. Furthermore, the information extracted from

a detected gravitational wave signal would be strongly attached to the properties of the detector, or the network of detectors, available.

In this thesis, we have seen that GW150914 could be described using different configurations of the black hole binary. The construction of the waveforms coming from these configurations is not worthless. The more waveforms templates coming from different configurations in the parameter space of the source, the more potential events we will detect. The requirements, in terms of accuracy of the templates, to detect a gravitational wave event, are also attached to the detector. In this thesis, we compute a single waveform with three different resolution, and we have seen that the actual LIGO detector, that is not yet at design sensitivity, could distinguish between the lower resolution waveform and the other two. When actual detectors reach design sensitivity, or future planned detectors are operational, leading to higher SNR detections, more accurate waveform models will be needed.

Bibliography

[1] R.A. Hulse and J.H. Taylor. Discovery of a pulsar in a binary system. *Astrophysical Journal*, 195:L51–L53, January 1975.

[2] R.V. Wagoner. Test for the existence of gravitational radiation. *Astrophysical Journal*, 196:L63–L65, March 1975.

[3] A. Einstein. The foundation of the general theory of relativity. *Annalen Phys*, 49:769–822, 1916.

[4] S.G. Hahn and R.W. Lindquist. Thw two-body problem in geometrodynamics. *Annals of Physics*, 29:304–331, September 1964.

[5] F. Pretorius. Evolution of binary black hole spacetimes. *Phys. Rev. Lett.*, 95:121101, September 2005.

[6] B. Abbot et al. Ligo: the laser interferometer gravitational-wave observatory. *Reports on Progress in Physics*, 72:076901, 2009.

[7] B. Caron et al. The virgo interferometer. *Classical and Quantum Gravity*, 14(6):1461, 1997.

[8] H. Lück et al. The geo600 project. *Classical and Quantum Gravity*, 14(6):1471, 1997.

[9] B. Abbot et al. Observation of gravitational waves from a binary black hole merger. *Phys. Rev. Lett.*, 116:061102, February 2016.

[10] B. Abbot et al. Properties of the binary black hole merger GW150914. *Phys. Rev. Lett.*, 116:241102, 2016.

[11] K. Schwarzschild. On the gravitational fiel of a mass point according to einstein's theory. *Sitzungsber.Preuss.Akad.Wiss.Berlin (Math.Phys)*, pages 189–196, 1916.

[12] C.W. Misner, K.S. Thorne, and J.A. Wheeler. *Gravitation.* W.H.Freeman, 1973.

[13] K.D. Kokkotas and B.G Schmidt. Quasi-normal modes of stars and black holes. *Living Reviews in Relativity*, 2(2), 1999.

[14] W.H. Press. Long wave trains of gravitational waves from a vibrating black hole. *The Astrophysical Journal*, 171:L105–L108, 1971.

[15] B. Allen, O. Birnholtz, S. Ghosh, A. Nielsen, and A.G. Wiseman. GW150914: Simple arguments why it is a binary black hole. *LIGO Document*, T1500566, 2016.

[16] M. Maggiore. *Gravitational Waves. Volume 1: Theory and Experiments.* Oxford University Press, 2008.

[17] A. Buonanno and T. Damour. Effective one-body approach to general relativistic two-body dynamics. *Phys. Rev. D*, 59, March 1999. arXiv:gr-qc/9811091.

[18] A. Buonanno and T. Damour. Transition from inspiral to plunge in binary black hole coalescences. *Phys. Rev. D*, 64, November 2001. arXiv:gr-qc/0001013.

[19] T. Damour. Coalescence of two spinning black holes: An effective one-body approach. *Phys. Rev. D*, November 2001. arXiv:gr-qc/0103018.

[20] A. Buonanno, Y. Chen, and T. Damour. Transition from inspiral to plunge in precessing binaries of spinning black holes. *Phys. Rev. D*, 74, November 2006. arXiv:gr-qc/0508067.

[21] L. Lehner. Numerical relativity: A review. *Class. Quant. Grav.*, 18(17), 2001.

[22] J. Winicour. Characteristic evolution and matching. *Living Rev. Rel.*, 1, 1998.

[23] O.A. Reula. Hyperbolic methods for einstein's equations. *Living Rev. Relativity*, 1(3), 1998.

[24] R.M. Wald. *General Relativity.* University of Chicago Press, 1984.

[25] M. Alcubierre. *Introduction to 3+1 Numerical Relativiy.* Oxford Univ. Press, 2008.

[26] T. Baumgarte. Numerical relativity, 2013. International Centre of Theoretical Sciences, India.

[27] E. Gourgoulhon. 3+1 formalism and bases of numerical relativity. Laboratoire Univers et Thories, Observatoire de Paris, March 2007.

[28] R. Arnowitt, S. Deser, and W. Misner. Dynamical structure and definition of energy in general relativity. *Phys. Rev.*, 116:1322, December 1959.

[29] T. Nakamura, K. Oohara, and Y. Kojima. General relativistic collapse to black holes and gravitational waves from black holes. *Progress of Theoretical Physics Supplement*, 90:1–218, 1987.

[30] T. Baumgarte and S.L. Shapiro. Numerical integration of einstein's field equations. *Phys. Rev. D*, 59, December 2008.

[31] M. Shibata and T. Nakamura. Evolution of three-dimensional gravitational waves: Harmonic slicing case. *Phys. Rev. D*, 52, November 1995.

[32] J.W. York. *Kinematics and dynamics of general relativity.* Smarr, L.L., 1979.

[33] B. Brügmann, J.A. González, M. Hannam, S. Husa, U. Sperhake, and W. Tichy. Calibration of moving puncture simulations. *Phys. Rev. D*, 77, January 2008.

[34] F. Löffler, J. Faber, E. Bentivegna, T. Bode, P. Diener, R. Haas, I. Hinder, B.C. Mundim, C.D. Ott, E. Schnetter, G. Allen, M. Campanelli, and P. Laguna. The einstein toolkit: A community computational infrastructure for relativistic astrophysics. *arXiv:1111.3344v1 [gr-qc]*, November 2011.

[35] U. Sperhake. Black-hole binary evolutions with the lean code. *Journal of Physics: Conference Series*, 66(1), 2007.

[36] C. Bona, C. Palenzuela-Luque, and C. Bona-Casas. *Elements of Numerical Relativity and Relativistic Hydrodynamics: From Einstein's Equations to Astrophysical Simulations.* Springer, Berlin Heidelberg, 2009. DOI 10.1007/978-3-642-01164-1.

[37] U. Sperhake. Numerical relativity breakthrough for binary black holes. *arXiv:1411.3997v1 [gr-qc]*, November 2014.

[38] M.J. Berger and J. Oliger. Adaptative mesh refinement for hyperbolic partial differential equations. *J. Comput. Phys.*, 53, 1984.

[39] M. Campanelli, C.O. Lousto, P. Marronetti, and Y. Zlochower. Accurate evolutions of orbiting black-hole binaries without excision. *Phys. Rev. Lett.*, 96, March 2006.

[40] B. Mongwane. Toward a consistent framework for high order mesh refinement schemes in numerical relativity. *General Relativity and Gravitation*, 47(5), 2015.

[41] Y. Wiaux, L. Jacques, and P. Vandergheynst. Fast spin +-2 spherical harmonics transforms and application in cosmology. *astro-ph/0508514*, 2005.

[42] J. Thornburg. Event and apparent horizon finders for 3+1 numerical relativity. *Living Rev. Rel.*, 10, 2007.

[43] R. Arnowitt, S. Deser, and C. Misner. *Gravitation: an introduction to current research.* New York: John Wiley, 1962.

[44] P. Diener and F.S. Guzmán. The wave equation in 1+1, April 2013. Lecture notes.

[45] S. Husa. Numerical modelling of black holes as sources of gravitational waves in a nutshell. *arXiv:0812.4395v1 [gr-qc]*, 2008.

[46] R. Courant, K. Friedrichs, and H. Lewy. On the partial difference equations of mathematical physics. *IBM Journal of Research and Development*, 11, 1967.

[47] S. Husa, M. Hannam, J.A. González, U. Sperhake, and B Brügmann. Reducing eccentricity in black-hole binary evolutions with initial parameters from post-newtonian inspiral. *Phys. Rev. D*, 77:044037, February 2008.

[48] Inc. Wolfram Research. *Mathematica.* Wolfram Research, Inc, version 10.4 edition, 2016.

[49] https://www.bsc.es/marenostrum-support-services.

[50] L.F. Richardson. The approximate arithmetical solution by finite differences of physical problems involving differential equations, with an application to the stresses in a masonry dam. *Philosophical Transactions of the Royal Society of London A: Mathematical, Physical and Engineering Sciences*, 201(459-470):307–357, 1911.

[51] T.A. Apostolatos, C. Cutler, G.J. Sussman, and K.S. Thorne. Spin-induced orbital precession and its modulation of the gravitational waveforms from merging binaries. *Phys. Rev. D*, 49(12), June 1994.

[52] M. Hannam. Modelling gravitational waves from precessing black-hole binaries: progress, challenges and prospects. *General Relativity and Gravitation*, 46(9):1–20, 2014.

[53] P. Schmidt, M. Hannam, S. Husa, and P. Ajith. Tracking the precession of the compact binaries from their gravitational-wave signal. *Phys. Rev. D*, 84:024046, 2011.

[54] J.A. Gonzázel, U. Sperhake, B. Brügmann, M. Hannam, and S. Husa. Total recoil: the maximum kick from nonspinning black-hole binary inspiral. *Phys. Rev. Lett.*, 98:091101, February 2007.

[55] F. Herrmann, I. Hinder, D. Shoemaker, P. Laguna, and R.A. Matzner. Gravitational recoil from spinning binary black hole mergers. *The Astrophysical Journal*, 661(1):430, 2007.

[56] D. Koppitz, D. Pollney, C. Reisswig, L. Rezzolla, J. Thornburg, P. Diener, and E. Schnetter. Recoil velocities from equal-mass binary-black-hole mergers. *Phys. Rev. Lett.*, 99:041102, July 2007.

[57] González, J.A. and Hannam, M. and Sperhake, U. and Brügmann, B. and Husa, S. Supermassive recoil velocities for binary black-hole mergers with antialigned spins. *Phys. Rev. Lett.*, 98:231101, June 2007.

[58] C. Reisswig and D. Pollney. Notes on the integration of numerical relativity waveforms. *Class. Quant. Grav.*, 28:195015, September 2011.

[59] http://lisa.nasa.gov/.

[60] Miquel Trias Cornellana. *Gravitational wave observation of compact binaries: Detection, parameter estimation and template accuracy.* PhD thesis, Universitat de les Illes Balears, Departament de Física, 2010.

[61] https://www.ligo.caltech.edu/WA.

[62] https://www.ligo.caltech.edu/LA.

[63] http://www.stargazing.net/kepler/altaz.html.

[64] M. Luna and A.M. Sintes. Parameter estimation of compact binaries using the inspiral and ringdown waveforms. *Classical and Quantum Gravity*, 23(11):3763, 2006.

[65] https://losc.ligo.org/tutorials/.

[66] Waveform: SXS:BBH:0305. Available for download at http://www.black-holes.org/waveforms.

[67] M. Hannam, S. Husa, J.G. Baker, M. Boyle, B. Brügmann, T. Chu, N. Dorband, F. Herrmann, I. Hinder, B.J. Kelly, L.E. Kidder, P. Laguna, K.D. Matthews, J.R. van Meter, H.P. Pfeiffer, D. Pollney, C. Reisswig, M.A. Scheel, and D. Shoemaker. Samurai project: Verifying the consistency of black-hole-binary waveforms for gravitational-wave detection. *Phys. Rev. D*, 79:084025, April 2009.

[68] L. Lindblom, B.J. Owen, and D.A. Brown. Model waveform accuracy standards for gravitational wave data analysis. *Phys. Rev. D*, 78:124020, December 2008.

[69] B. Abbott et al. Gw150914: First results from the search for binary black hole coalescence with advanced ligo. *Phys. Rev. D*, 93:122003, June 2016.

[70] B. Allen, W.G. Anderson, P.R. Brady, D.A. Brown, and J.D.E. Creighton. Findchirp: An algorithm for detection of gravitational waves from inspiraling compact binaries. *Phys. Rev. D*, 85:122006, June 2012.